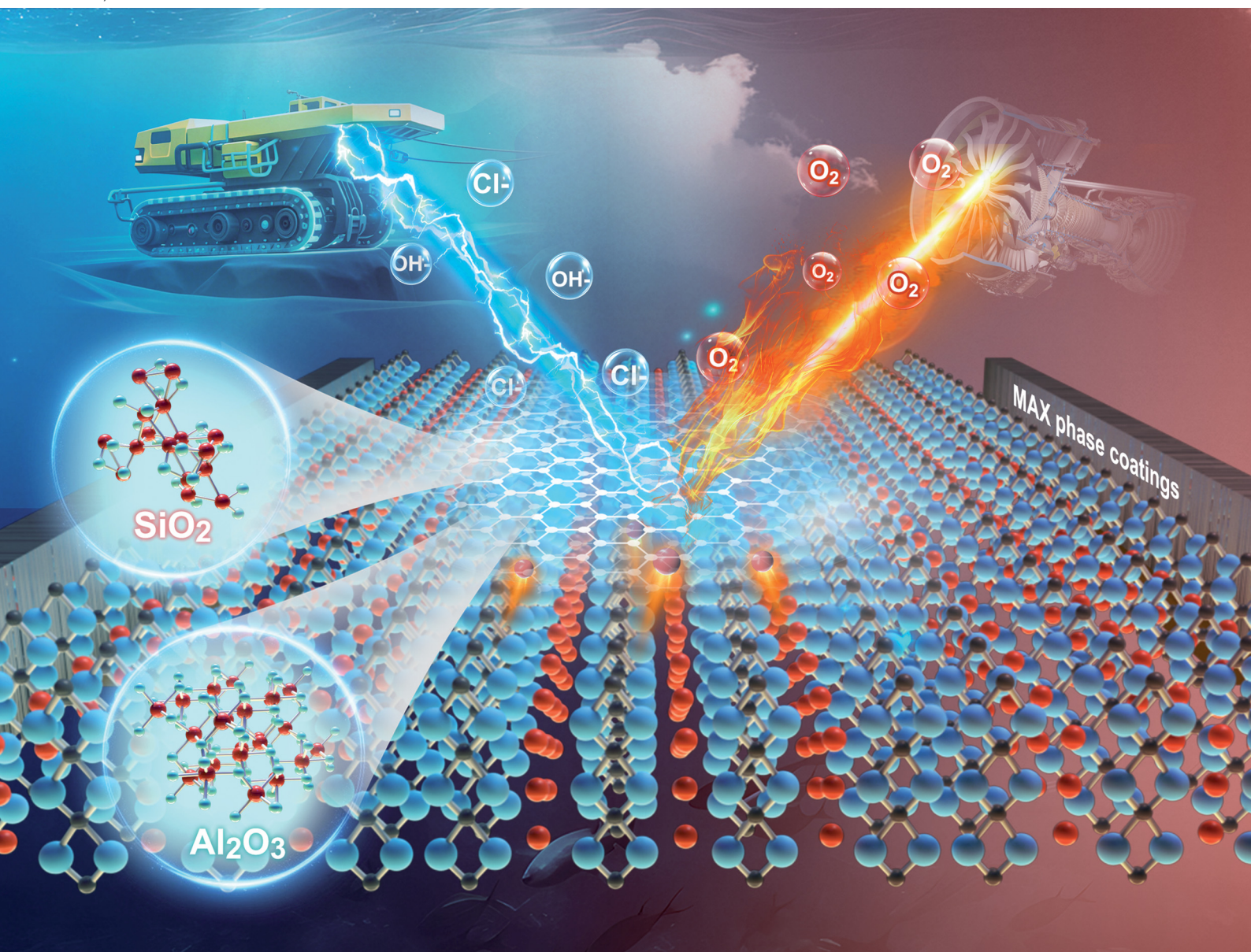


# Materials Horizons

Volume 12  
Number 6  
21 March 2025  
Pages 1679–2026

[rsc.li/materials-horizons](https://rsc.li/materials-horizons)



ISSN 2051-6347



## REVIEW ARTICLE

Zhenyu Wang, Aiyang Wang *et al.*  
MAX phase coatings: synthesis, protective performance, and  
functional characteristics

## REVIEW

[View Article Online](#)  
[View Journal](#) | [View Issue](#)Cite this: *Mater. Horiz.*, 2025,  
12, 1689

## MAX phase coatings: synthesis, protective performance, and functional characteristics

Guanshui Ma, Anfeng Zhang, Zhenyu Wang, \* Kaihang Wang, Jiayue Zhang, Kaixuan Xu, Yuxi Xu, Shenghao Zhou and Aiyang Wang \*

$M_{n+1}AX_n$  (MAX) phases are a novel class of materials with a closely packed hexagonal structure that bridge the gap between metals and ceramics, garnering tremendous research interest worldwide in recent years. Benefiting from their unique layered structure and mixed covalent–ionic–metallic bonding characteristics, MAX phase coatings possess excellent oxidation resistance, and exceptional electrical and thermal conductivities, making them highly promising for applications in advanced nuclear materials, battery plate protection materials, and aero-engine functional materials. This review aims to provide a comprehensive understanding of MAX phase coatings. It presents an overview of their compositions and microstructure, highlighting well-established structures like 211, 312, and 413. Furthermore, it delves into the various synthesis methods employed in fabricating MAX phase coatings, including physical vapor deposition, chemical vapor deposition, spraying methods, and laser cladding, among others. The potential applications of MAX phase coatings, high-temperature oxidation resistance, mechanical protection, salt spray corrosion resistance, etc., are also investigated. Finally, this review discusses the future potential of MAX phase coatings and proposes areas for further research and improvement. The primary goal is to offer theoretical guidance and innovative ideas for the synthesis and development of superior MAX phase coatings for commercial applications.

Received 30th July 2024,  
Accepted 13th December 2024

DOI: 10.1039/d4mh01001a

[rsc.li/materials-horizons](https://rsc.li/materials-horizons)

## Wider impact

The synthesis and application of MAX phase coatings have attracted significant attention in materials science due to their unique metallic and ceramic properties. This review on their synthesis, protective performance, and functional characteristics broadens our understanding and potential advancements in several critical areas. The theoretical insights and innovative synthesis methods discussed pave the way for future research and development. By exploring new compositions and techniques, researchers can enhance the properties of MAX phase coatings, making them more versatile and effective. MAX phase coatings offer exceptional resistance to high-temperature oxidation and corrosion, making them ideal for extreme environments such as marine and nuclear fields. Understanding the oxidation and corrosion mechanisms discussed provides valuable insights for designing high-performance coatings. This review also summarizes the functional protective capabilities of MAX phase coatings in electrical conductivity, corrosion resistance, and electromagnetic shielding, and highlights their properties as radiation-resistant nuclear cladding and interfacial layers for thermal barrier coatings. This opens new avenues for applications in electronics, advanced energy, and aerospace sectors, driving innovation and contributing to more sustainable and efficient industrial practices.

## 1. Introduction

In the 1960s, Nowotny<sup>1</sup> and his group in Vienna discovered more than 100 new carbides and nitrides. Among these, over 30 had similar layered hexagonal structures, known initially as Hagg phases, characterized by  $M_2X$  layers interspersed with pure A layers. The significant breakthrough that reignited interest in these materials occurred in the mid-1990s when

Barsoum *et al.*<sup>2</sup> synthesized relatively phase-pure samples of  $Ti_3SiC_2$ . However, in 2000 the Hagg phase was renamed  $M_{n+1}AX_n$  (MAX), where M represents a transition metal element mainly including Ti, Nb, Zr, Hf, V, Mo, Ta and Cr,<sup>3</sup> the A sites are occupied by elements from group IIIA or IVA, such as Al, Si, and Ge, and also included post-transition metal elements like Au, Ir, and Zn, while X was C or N.<sup>4</sup> In 2011,<sup>5</sup> the first 2D transition metal carbide ( $Ti_3C_2$ ), known as “MXene”, was synthesized by selectively etching Al atoms from the  $Ti_3AlC_2$  MAX phase, which further stimulated the development of MAX phases.<sup>6–10</sup> Subsequently, the structures of in-plane MAX (*i*-MAX) and out-of-plane (*o*-MAX) were studied from both

Key Laboratory of Advanced Marine Materials, Ningbo Institute of Materials Technology and Engineering, Chinese Academy of Sciences, Ningbo, 315201, China.  
E-mail: wangzy@nimte.ac.cn, aywang@nimte.ac.cn



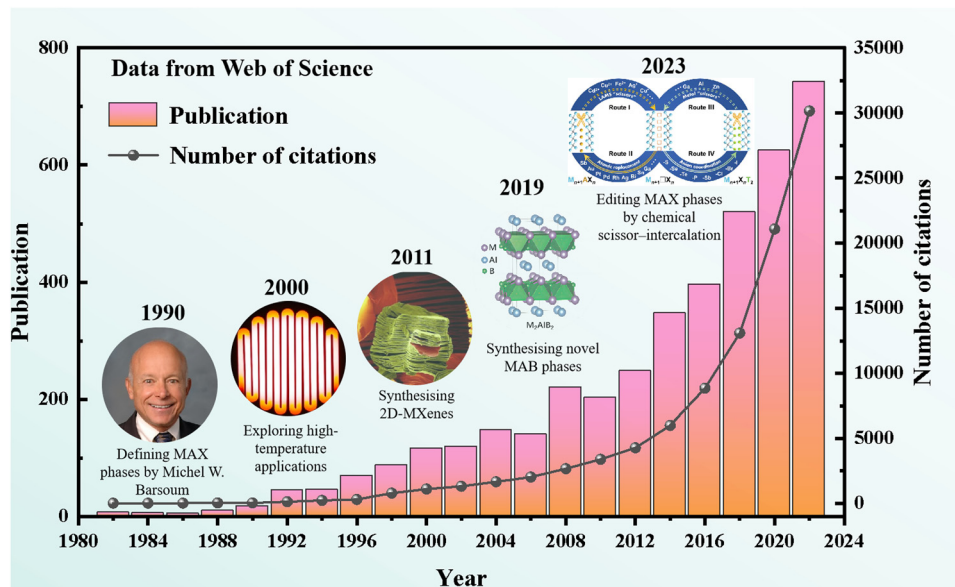


Fig. 1 History and research trends of MAX phases.

experimental and theoretical simulation calculations.<sup>11–13</sup> Fig. 1 illustrates the history and research trends of MAX phases.

All reported MAX phases were C-based or N-based MAX systems until 2019, when Ade *et al.*<sup>14</sup> attempted to synthesize a new MAX phase by introducing B as the X element. The first stable B-based (X site) MAX phase was prepared by Wang *et al.*<sup>15</sup> Recently, the X site element expanded to P and Se,<sup>16</sup> and the M site elements have been extended from transition metals (including Mn, Fe, Co, Ni, Cu, and Zn) to rare-earth elements, including Ce, Pr, Nd, Sm, Gd, Tb, Dy, Ho, Er, Tm and Lu.<sup>17–19</sup> Moreover, the discovery of new solid-solution MAX phases has allowed for the incorporation of more elements into ternary MAX phases, significantly expanding the MAX phase family. Meanwhile, since the positions of oxygen and carbon peaks perfectly match with each other, oxygen was identified as a potential X element in the MAX.<sup>20</sup> Additionally, the medium-entropy MAX phases composed of 3 elements mixed at a specific site and high-entropy phases formed by correspondingly mixing equal or relatively large proportions of 4 or more elements were found, which also promoted the diversity of MAX phases.<sup>21–29</sup> In 2023, Huang *et al.*<sup>30</sup> discovered a series of layered carbonitride materials with new structure and composition characteristics by using the universal “chemical scissors” structure editing strategy, which further expanded the types of MAX phases. Recently, Dahlqvist *et al.* identified 182 new theoretically stable MAX phases by calculation of phase stability.<sup>31</sup> Fig. 2 provides an overview of the elements constituting the MAX phases, which encompass both solid solution and chemical order, and covers a significant portion of the periodic table. Specifically, it includes 28 different elements for the M-site, 28 elements for the A-site, and 6 elements for the X-site.

Depending on the value of  $n$ , the  $M_{n+1}AX_n$  phases were initially classified into 211, 312, and 413 phases.<sup>32</sup> These MAX phases all have layered hexagonal structures with space group  $P63/mmc$  (No. 194), consisting of  $M_6X$  octahedra separated by A atomic layers.<sup>33</sup>

M–X bonds in  $M_6X$  octahedra are strong covalent bonds, while the M–A bonds between the  $M_6X$  layers and the A atomic layer are much weaker, particularly in shear.<sup>34</sup> The primary structural differences among the 211, 312 and 413 phases lie in the number of  $M_6X$  layers separating the A layers. As illustrated in Fig. 3a, two, three and four  $M_6X$  layers exist in between every two A layers in the 211, 312 and 413 phases crystal structures, respectively. Another distinction among the three crystal structures is their polymorphism: the 211 phase has one polymorph, the 312 phase has two polymorphs ( $\alpha$  and  $\beta$ ), and the 413 phases have three ( $\alpha$ ,  $\beta$  and  $\gamma$ ), as shown in Fig. 3b. The polymorphs differ slightly in the atomic stacking sequences of the M–X blocks.<sup>35</sup> With ongoing research into MAX phases, the family has expanded to include higher-order phases such as the 514, 615, and 716 series.<sup>36–38</sup>

Over the last few decades, MAX phases have garnered considerable interest from researchers, due to their unique combination of both metallic and ceramic characteristics.<sup>37,39</sup> The study of MAX phases has been systematically and extensively investigated, ranging from theoretical models to experimental validations,<sup>40–42</sup> and from structural design to performance evaluation.<sup>17,43–45</sup> Particularly, thanks to their unique layered structure and atomic bond characteristics, MAX phase coatings, which have been developed since 2004, exhibit outstanding damage tolerance,<sup>46–48</sup> excellent corrosion/oxidation resistance,<sup>49,50</sup> remarkable mechanical properties,<sup>51,52</sup> and high electrical conductivity.<sup>53,54</sup> These superior advantages highlight the potential applications of MAX phases as protective coatings for vital components in severe environments,<sup>55</sup> such as advanced nuclear materials,<sup>54,56</sup> battery plate protection materials,<sup>57,58</sup> and aero-engine functional materials.<sup>59</sup> Fig. 4 shows the potential applications, properties, and common preparation methods of MAX phase coatings. Benefiting from the tremendous contribution of researchers worldwide, numerous innovative synthesis methodologies and novel microstructures of MAX phase coatings have been documented in recent

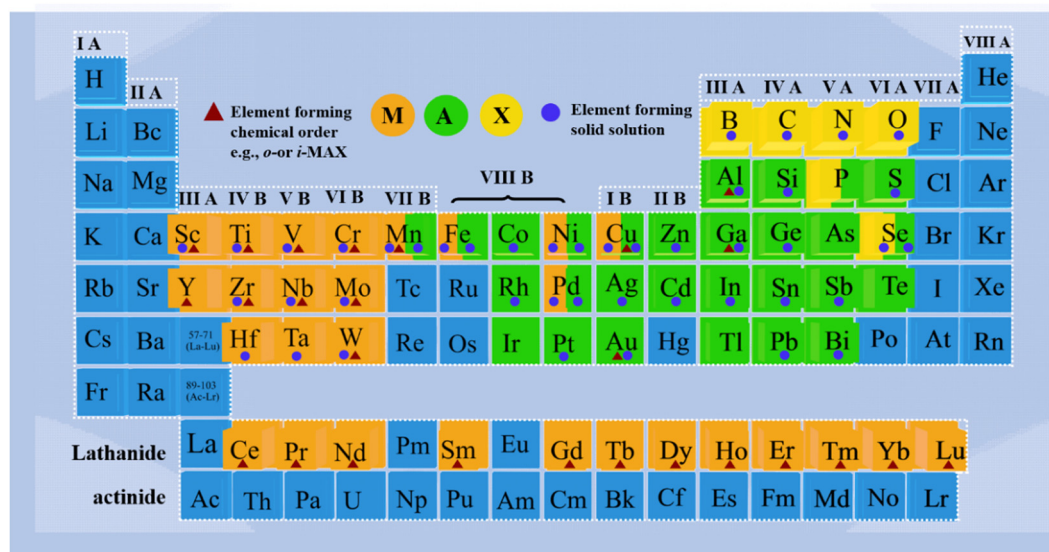


Fig. 2 The corresponding positions of MAX phase elements in the periodic table of chemical elements. Reproduced and adapted with permission.<sup>31</sup> Copyright 2023 Elsevier Ltd.

years. Here, we summarize the synthesis techniques and prospective application domains utilized in the creation of MAX phase coatings, alongside the ongoing research endeavors to elucidate their physical properties and viable commercial utilization.

## 2. Preparation methods of MAX phase coatings

### 2.1. Physical vapor deposition

Physical vapor deposition (PVD) is a widely used method for preparing various MAX phase coating systems, known for its low operating temperature, convenient equipment operation, environmentally friendly nature, and the ability to achieve

large-area preparation.<sup>60,61</sup> In the fabrication of MAX phase coatings, popular PVD techniques mainly include magnetron sputtering, cathodic arc deposition and pulse laser deposition.

**2.1.1 Magnetron sputtering.** Magnetron sputtering (MS) generates plasma by supplying current and voltage through a direct current (DC) power source, causing the target material to release metal ions that deposit onto the substrate to form a coating.<sup>62</sup> Li *et al.*<sup>63</sup> successfully prepared high-purity  $\text{Ti}_2\text{AlC}$  and  $\text{Ti}_3\text{AlC}_2$  coatings by conducting DCMS at room temperature and subsequently annealing them at 800 °C. Abbas *et al.*<sup>64</sup> employed medium-frequency MS to deposit a  $\text{Ti}_2\text{AlC}$  MAX phase on a stainless-steel substrate, achieving a one-step transformation of the  $\text{Ti}_2\text{AlC}$  MAX phase at a lower substrate temperature of 750 °C. The coatings were uniform, dense,

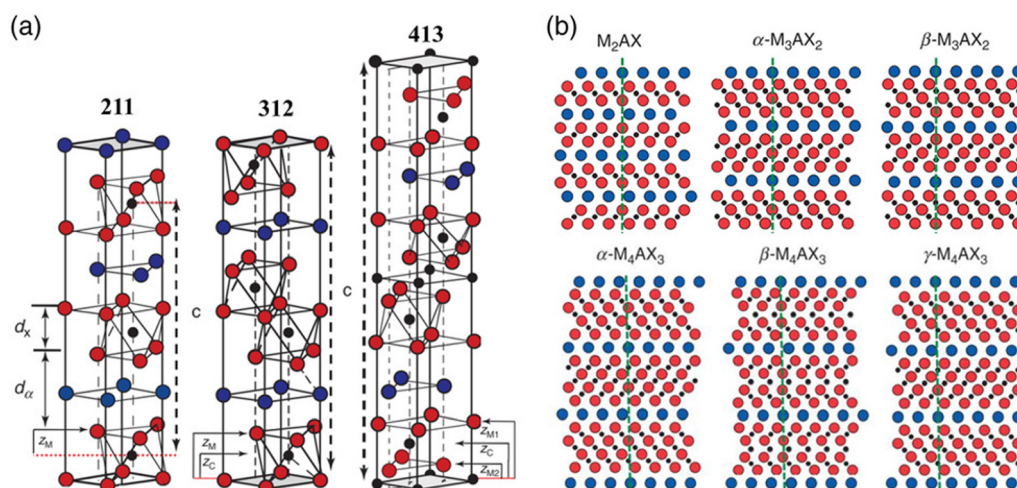


Fig. 3 Crystal structure of 211, 312, and 413 MAX phases. (a) Unit cell of the three phases. The lattice parameter  $c$  of each unit cell is outlined by vertical dashed lines. The thicknesses of the  $\text{M}_6\text{X}$  layer and A layer are denoted as  $d_x$  and  $d_a$ , respectively. (b) Schematics of the  $[11\bar{2}0]$  planes and the polymorphism of the MAX phases. Reproduced with permission.<sup>35</sup> Copyright 2020 Wiley-VCH GmbH.



Fig. 4 Potential applications, properties and common preparation methods of MAX phase coatings.

and free from cracks, with significantly enhanced electrical conductivity.

Furthermore, high power impulse magnetron sputtering (HiPIMS) is a novel magnetron sputtering technique that overcomes the limitations of insufficient heat capacity in traditional magnetron sources by utilizing high peak power and low duty cycle (1–10%), enabling operation at high power levels and short pulse widths (50–200  $\mu\text{s}$ ).<sup>65</sup> During the fabrication process, HiPIMS allows for adjustable plasma density (up to  $10^{18}$ – $10^{19}$   $\text{m}^{-3}$  near the target), ionization rate ( $\geq 30\%$ ) and deposition particle energy, offering significant controllability.<sup>66</sup>

Li and co-authors<sup>67</sup> deposited Ti–Al–C coatings on a Ti–6Al–4V substrate using the HiPIMS technique. Experimental results demonstrated that HiPIMS, with its high ionization plasma flux and high kinetic energy, facilitated the formation of nanostructured  $\text{TiAl}_x$  compounds. After a low-temperature annealing step at 700 °C, HiPIMS promoted the generation of dense and smooth  $\text{Ti}_3\text{AlC}_2$  phase coatings. Fig. 5 shows a schematic illustration of HiPIMS synthesis of the  $\text{Ti}_3\text{AlC}_2$  MAX phase coating. The sufficiently high ion energy provided by HiPIMS supported the continuous growth of the coatings, resulting in a denser microstructure and relatively stronger adhesion. Zhang *et al.*<sup>68</sup> utilized HiPIMS to prepare Ti–Al–N coatings from a

$\text{Ti}_2\text{AlN}$  composite target. The coatings, composed of MAX-phase  $\text{Ti}_2\text{AlN}$  and tetragonal  $\text{Ti}_2\text{N}$  phases, were obtained at a temperature of 450 °C, exhibiting a stable coating structure after vacuum annealing at 800 °C. Recently, Zhou *et al.*<sup>69</sup> also obtained highly crystallized  $\text{Cr}_2\text{AlC}$  MAX phase coatings on a Ti–6Al–4V substrate at a temperature as low as 480 °C using a hybrid DCMS/HiPIMS technique (Fig. 6a and b). The research revealed that  $\text{Cr}_2\text{AlC}$  MAX phase coatings deposited within the temperature range of 480–530 °C consisted of uniform, densely packed, and randomly oriented grains (Fig. 6c and d), but started to decompose at 800 °C. Moreover, the hybrid DCMS/HiPIMS technique resulted in a calculated surface temperature increment of approximately 122 °C, with Cr and Ar ions/atoms contributing 64% and 31% of the total energy flux, respectively.

The HiPIMS technique significantly enhances the diffusion of adsorbed atoms on the surface of coatings, thereby improving their density and protective capabilities. This makes HiPIMS crucial for future PVD deposition coatings. However, variations in HiPIMS process parameters can substantially impact coating properties. Zhou *et al.*<sup>70</sup> utilized HiPIMS to fabricate Ti–Al–C coatings at different deposition pressures, observing that as the pressure increased, the thickness and deposition rate of the coatings initially rose and then declined.



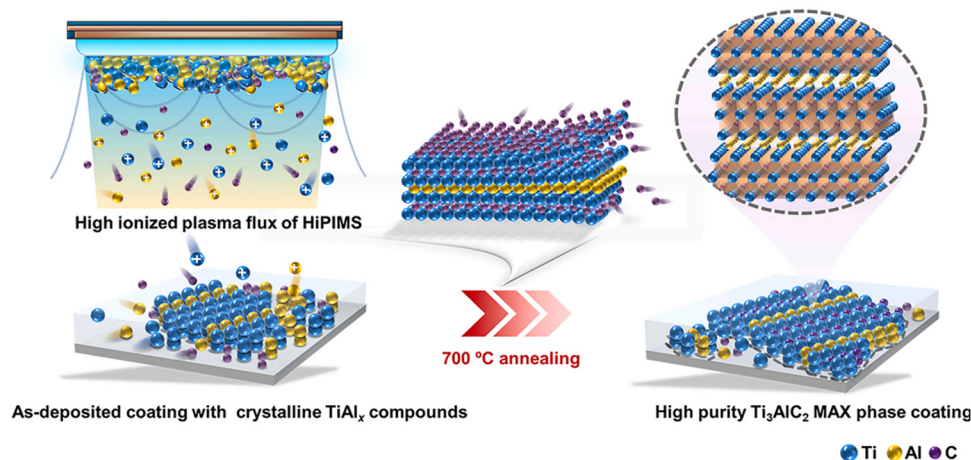


Fig. 5 Schematic illustration for low temperature synthesis of HiPIMS induced  $\text{Ti}_3\text{AlC}_2$  MAX phase coatings. Reproduced with permission.<sup>67</sup> Copyright 2023 Elsevier Ltd.

Qureshi *et al.*<sup>71</sup> conducted a comparative study on the influence of different frequencies (1.2–1.6 kHz) and pulse widths (20–60  $\mu\text{s}$ ) of average power on  $\text{Cr}_2\text{AlC}$  MAX phase coatings. The results demonstrated that the pulse width had a more pronounced effect on enhancing the compactness of coatings in HiPIMS compared to the frequency. Therefore, further research is essential to investigate how deposition process parameters such as pulse width, frequency, and bias voltage affect the coating structure, performance, and other characteristics.

Magnetron sputtering is the most commonly used PVD method due to the easy processing, high flexibility, good

control over phase purity and composition, and the smooth coating surface. However, the coating prepared by this method has a low rate, and the required time is relatively long when the thickness of the prepared coating is large. In addition, the coating prepared by this method is limited by the substrate material, and a transition layer is often needed to improve the bonding strength.

**2.1.2 Cathodic arc deposition.** Cathodic arc deposition involves generating high-intensity arc discharges on the cathode surface, which heats and evaporates the cathode material. The resulting high-energy ions and neutral atoms then deposit

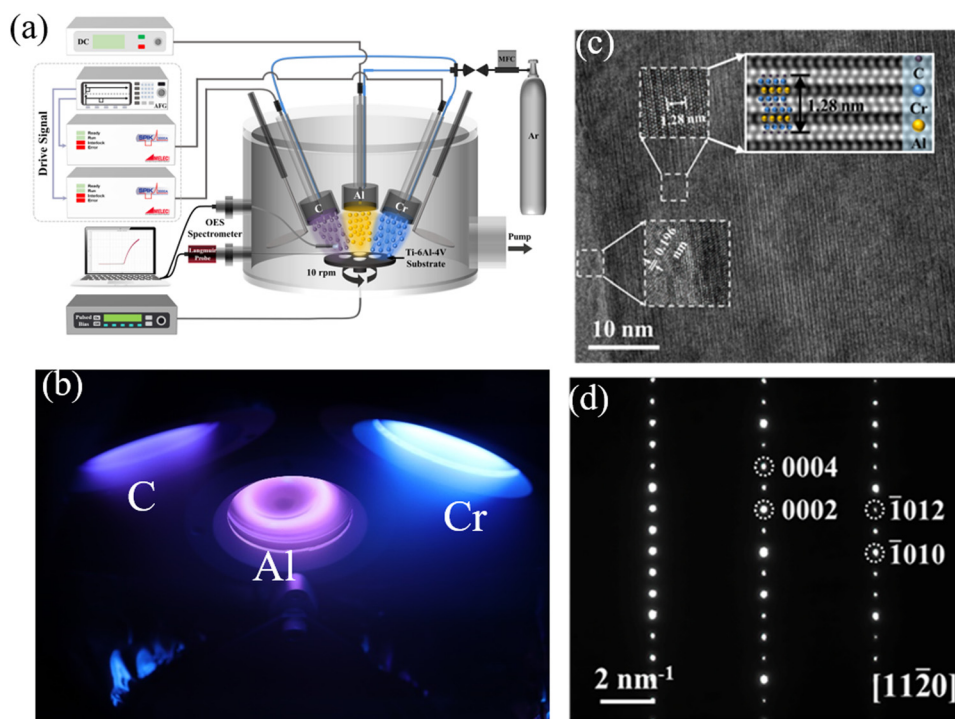


Fig. 6 (a) Schematic diagram of the hybrid DCMS/HiPIMS deposition system used, (b) physical images of three target materials during operation, (c) HRTEM images and the Fourier filter of the Cr–Al–C coating at 480 °C, and (d) the SAED pattern of the Cr–Al–C coating at 480 °C. Reproduced and adapted with permission.<sup>69</sup> Copyright 2024 Elsevier B.V.

onto the substrate surface, forming the coating. The heat and energy released by the arc during the fabrication process facilitate diffusion and interaction between the coating material and the substrate, thus achieving a strong bond between them.<sup>72</sup>

Rosen *et al.*<sup>73</sup> fabricated Ti<sub>2</sub>AlC coatings using the high-current pulsed cathodic arc deposition method. They employed three independent cathodes to deposit epitaxial coatings under alternating plasma pulses at 900 °C, allowing for high-level control over the deposition material flux ratio. Li and co-authors<sup>74</sup> utilized filtered cathode vacuum arc deposition to deposit Ti<sub>3</sub>AlC<sub>2</sub> coatings at room temperature, followed by annealing at 800 °C for 1 h. The prepared coatings exhibited a smooth and dense structure with a significant reduction in surface micro-particles. Guenette *et al.*<sup>75</sup> successfully produced directionally oriented Ti<sub>2</sub>AlC coatings using pulsed cathodic arc deposition through various ratios of Ti:Al:C, achieving this without the need for a TiC<sub>x</sub> seed layer. In a separate study conducted by Mahmoudi *et al.*,<sup>76</sup> the arc method was employed to generate Ti<sub>2</sub>AlC and Ti<sub>3</sub>AlC<sub>2</sub> MAX phase coatings in a mixed gas environment of C<sub>2</sub>H<sub>2</sub>/Ar following an annealing treatment. The research findings revealed that annealing the coatings at 900 °C increased the content of Ti<sub>2</sub>AlC and Ti<sub>3</sub>AlC<sub>2</sub>, thus improving the overall deposition effect. The optimal deposition effect was observed when maintaining a volume ratio of 1/4 for C<sub>2</sub>H<sub>2</sub>/Ar. It is crucial to have a sufficient volume of C<sub>2</sub>H<sub>2</sub> during the deposition process, as excessively low levels can result in carbon deficiency, ultimately impeding the formation of Ti<sub>2</sub>AlC and Ti<sub>3</sub>AlC<sub>2</sub> MAX phases.

Cathodic arc deposition is known for its high cathodic deposition rate and low production cost, which enables rapid preparation of coatings and enhances the adhesion between the coating and the substrate. However, the prepared coatings often have large particles on the surface of the coating, resulting in an uneven coating surface. Therefore, the advantages of cathodic arc deposition and magnetron sputtering can be combined to prepare excellent coatings.

**2.1.3 Combined arc/sputtering deposition.** Combined arc/sputtering deposition is a technique that combines arc discharge and magnetron sputtering techniques. It involves applying high voltage between the anode and cathode to generate arc discharge. The high temperature and energy generated by the arc discharge cause the anode material to evaporate or ionize, and it is then deposited onto the substrate surface. Concurrently, a magnetic field is applied to control the ion trajectory, enhancing ion kinetic energy and impact energy, thus improving the density and adhesion of the coating.

Wang *et al.*<sup>77</sup> innovated and developed the high ionization arc combined magnetron sputtering technique for the preparation of MAX phase coatings. In this method, the arc provides the M-element, the magnetron supplies the A-element, and reactive gases such as hydrocarbons are introduced. By combining this with heat treatment, high-purity and well-dense Cr<sub>2</sub>AlC MAX phase coatings were successfully obtained. The prepared Cr<sub>2</sub>AlC coatings exhibit an equiaxed grain structure without columnar crystals and possess high bonding strength with substrates such as titanium alloys. This makes MAX phase

coatings promising for high-temperature protection and corrosion resistance in harsh environments.

Based on the special crystallographic relationship between the MAX phase and M<sub>n+1</sub>X<sub>n</sub>, a two-step strategy of pre-constructing the M<sub>n+1</sub>X<sub>n</sub> precursor for the subsequent solid-state reaction with element A can also reduce the phase formation temperature of MAX phases. Wang *et al.*<sup>78,79</sup> used a cathodic arc/sputter system to deposit multilayer Cr-C/Al phases and subsequently conducted heat treatment to obtain the Cr<sub>2</sub>AlC, as shown in Fig. 7(a-c). Analysis of its formation mechanism revealed the alternating growth of (Cr, C)-rich and Al-rich layers. The multi-layer phase composition was initially CrC<sub>x</sub>, but after vacuum annealing, the internal diffusion of Al resulted in the blurring and disappearance of the multi-layer interface, and the thickness of the Al-rich layer decreased, forming the MAX phase. This revealed the lowest temperature synthesis process for the preparation of MAX coatings so far. The mechanism of the intercalation method was also found in the preparation of Ti<sub>2</sub>AlC,<sup>80</sup> and the atom diffusion during annealing illustrated in Fig. 7(d). The strategy employs a “building blocks” approach in crystallography, where the A atomic layer diffuses and inserts into the MX (111) twin boundaries under thermal driving forces, leading to the formation of the MAX phase. Importantly, this synthesis process effectively circumvents the formation of intermediate competitive phases, offering a novel approach for the low-temperature fabrication of high-purity MAX phases.

**2.1.4 Pulse laser deposition.** Pulse laser deposition (PLD) has been less explored than other PVD techniques despite its high potential and better scalability for depositing MAX phase coatings at temperatures below 300 °C. In this method, a high-power pulsed laser beam strikes a MAX phase target in a high-vacuum chamber, vaporizing the target material and depositing it onto a substrate maintained at a low temperature (25–800 °C).<sup>81</sup>

Hu *et al.*<sup>82</sup> prepared Ti<sub>3</sub>SiC<sub>2</sub> coatings with a friction coefficient of 0.2 in humid air and a hardness between 30 and 40 GPa using MS assisted PLD at near room temperature to 300 °C. To control the mirror system, which allowed the laser beam to randomly strike the target over the selected ablation area, beam steering was accomplished using a computer with 248 nm wavelength, 20 ns duration, 1–50 Hz rate and 200–600 mJ energy. A schematic illustration of the magnetron sputtering assisted pulsed laser deposition system is shown in Fig. 8. Lange and co-authors<sup>83</sup> employed PLD with a pulsed Nd:YAG laser to the synthesized Cr<sub>2</sub>AlC MAX phase coating on stainless steel (SS) substrates. The method demonstrated that the ion-beam has several significant effects on coating thickness and composition, concentration gradients within the coatings as well as on conductivity and hardness.

**2.1.5 Other methods of PVD.** Feng *et al.*<sup>84</sup> employed the direct current reactive magnetron sputtering technique to prepare Ti–Al–C coatings on austenitic SS surfaces, which subsequently transformed into the Ti<sub>2</sub>AlC phase through heat treatment. Using a TiAl alloy target and introducing hydrocarbon reactive gases, they successfully produced Ti<sub>2</sub>AlC coatings with a high purity of up to 90 wt%. This method offers a simple and easy-to-control process, eliminating the need for Ti<sub>2</sub>AlC

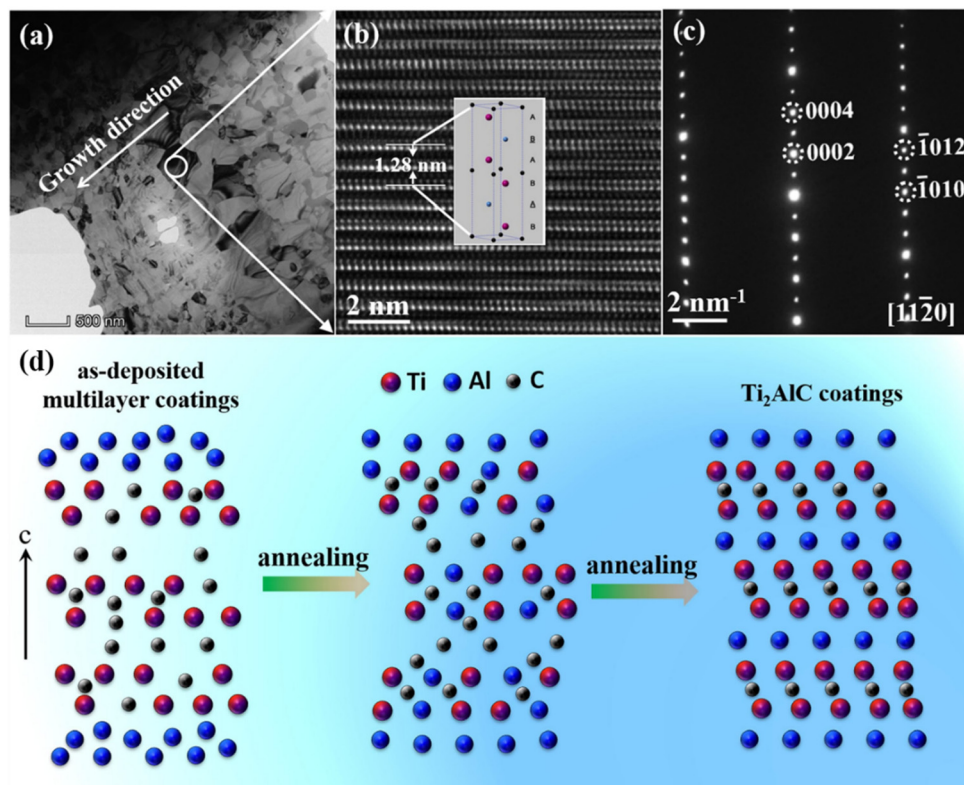


Fig. 7 (a) TEM bright-field image of the  $\text{Cr}_2\text{AlC}$  coating at low magnification. (b) HRTEM image of the grain within the round solid line in (a), and the inserted image showing the unit cell of  $\text{Cr}_2\text{AlC}$ . (c) The corresponding SAED with the electron beam parallel to the  $[11-20]$  direction. (d) Schematic diagram of a MAX phase coating prepared by depositing a precursor combined with a subsequent solid-phase reaction. Reproduced and adapted with permission.<sup>79,80</sup> Copyright 2020 Elsevier Ltd and 2019 Elsevier B.V.

MAX phase deposition targets and significantly reducing production costs. The prepared coatings exhibit a uniformly high-purity structure, expanding the compositional window of MAX phase coatings and broadening the range of substrate selection.

Ma *et al.*<sup>85</sup> fabricated amorphous Cr–Al–C coatings using a hybrid MS/cathodic arc deposition technique (Fig. 9a), and subsequently obtained the  $\text{Cr}_2\text{AlC}$  MAX phase by *in situ* heating TEM (Fig. 9b). Increasing the temperature from 25 to 370 °C led to the structural transformation from amorphous Cr–Al–C to crystalline  $\text{Cr}_2\text{Al}$  interphases, with the high-purity  $\text{Cr}_2\text{AlC}$  MAX phase distinctly forming at 500 °C, accompanied by the diminished amorphous feature. Similar phase evolution was also evidenced by the *ab initio* molecular dynamics calculations, where the bond energy of Cr–Cr, Cr–Al, and Cr–C played the key role in the formed crystalline stability during the heating process. Furthermore, Yuan *et al.*<sup>59</sup> also used sputtering/cathodic arc deposition and an *in situ* XRD technique to successfully prepare  $\text{M}_2\text{AlC}$  ( $\text{M} = \text{Ti}, \text{V}, \text{Cr}$ ) MAX phases. Compared to  $\text{V}_2\text{AlC}$  and  $\text{Cr}_2\text{AlC}$  MAX phase coatings, the  $\text{Ti}_2\text{AlC}$  coating displayed a higher phase-forming temperature, without any intermediate phases before the appearance of the  $\text{Ti}_2\text{AlC}$  MAX phase. The results of the first-principles calculations correlated with the experience in which  $\text{Ti}_2\text{AlC}$  exhibited the largest formation energy and density of states.

Bahraei *et al.*<sup>86</sup> developed a novel approach using a combination of PVD and post-laser treatment to successfully fabricate  $\text{Ti}_2\text{AlC}$  MAX phase coatings on Ti–6Al–4V alloy substrates. This

method involves an initial carbon coating treatment of the substrate using PVD, followed by Nd:YAG laser and semiconductor laser irradiation of the coating. Compared to the Ti–6Al–4V substrate, the wear rate of the laser-treated samples was reduced by approximately 81%, the average friction coefficient decreased by nearly 66%, and the hardness increased by 2.5 to 4.5 times. This method enhances the wear resistance and hardness of the coatings, further expanding their range of application.

## 2.2. Chemical vapor deposition

Chemical vapor deposition (CVD) is a method for forming coatings on a substrate surface through chemical reactions using gas-phase elemental or compound species containing the coating elements. This process involves temperatures that facilitate the diffusion of reactants on the substrate surface, and appropriate control of the reaction temperature ensures a strong bond between the coating and the substrate.

In 1972, Nickl *et al.*<sup>87</sup> successfully prepared  $\text{Ti}_3\text{SiC}_2$  coatings using a mixture of gases including  $\text{TiCl}_4$ ,  $\text{SiCl}_4$ ,  $\text{CCl}_4$ , and  $\text{H}_2$  at 1200 °C, demonstrating the feasibility of CVD for fabricating MAX phase coatings for the first time. Subsequently, researchers replaced  $\text{CCl}_4$  with  $\text{CH}_4$  as the carbon source and successfully prepared  $\text{Ti}_3\text{SiC}_2$  coatings.<sup>88</sup> Pickering *et al.*<sup>89</sup> utilized the CVD method to fabricate  $\text{Ti}_3\text{SiC}_2$ , obtaining a complex microstructure consisting of multiple phases such as  $\text{Ti}_3\text{SiC}_2$ , TiC, and  $\text{TiSi}_2$ .



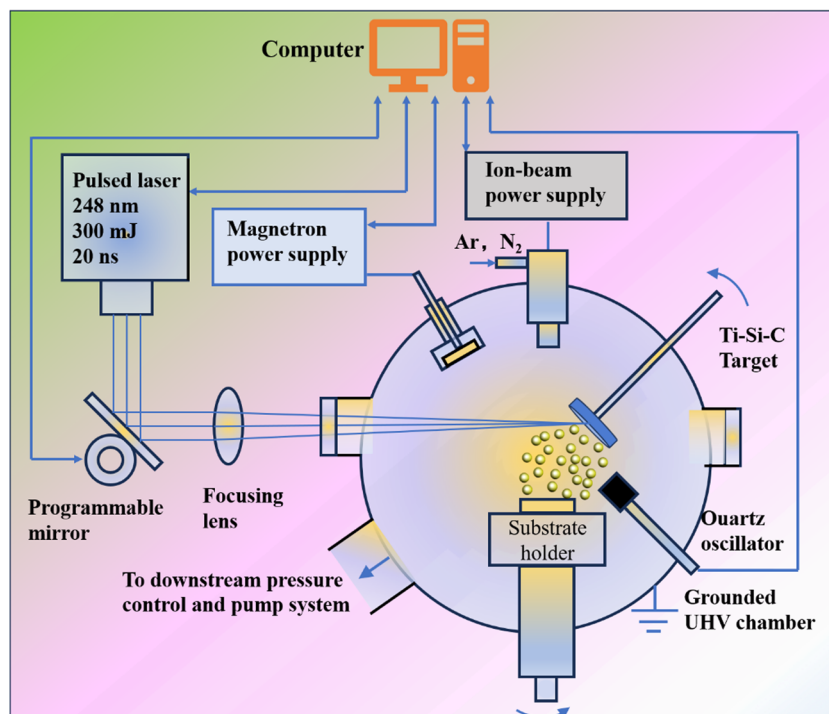


Fig. 8 Schematic illustration of the magnetron sputtering assisted pulsed laser deposition system. Reproduced and adapted with permission.<sup>82</sup> Copyright 2004 Plenum Publishing Corporation.

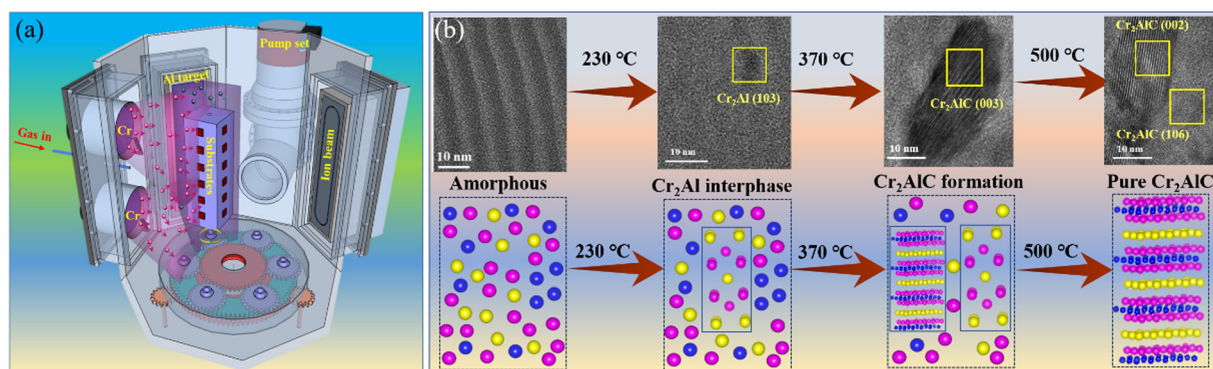


Fig. 9 (a) A schematic of the hybrid cathodic arc/magnetron sputtering process for depositing Cr-Al-C coatings. (b) Microstructure of TEM and schematic diagram evolution of the Cr-Al-C coating during *in situ* TEM heating. Reproduced and adapted with permission.<sup>85</sup> Copyright 2024 Elsevier Ltd on behalf of the editorial office of the Journal of Materials Science & Technology.

This provided a deeper understanding of the chemical vapor deposition evolution process for  $\text{Ti}_3\text{SiC}_2$ .

However, the process of fabricating MAX phase coatings using CVD methods is relatively complex, requiring strict control over parameters such as gas flow rate, temperature, and composition. This increases the difficulty of operation and the equipment costs. Additionally, there may be issues with gas contaminants during the deposition process, which not only degrade coating quality or affect equipment performance, but also pollutes the environment. Moreover, controlling phase purity is challenging in the CVD fabrication of MAX phase coatings. In addition, the temperature for preparing MAX phase

coatings by CVD deposition is relatively high, which can easily cause tempering of the substrate material and limit its application. Consequently, the widespread application of CVD techniques for producing MAX phase coatings is presently limited.

### 2.3. Spraying method

Thermal spraying is a process that involves melting the coating material using thermal energy and then spraying it onto the substrate surface through high-speed gas flow atomization. Molten or semi-molten droplets are sprayed onto the substrate surface, “splashing” to cool and form a layered microstructure.<sup>90</sup> Depending on the heat source used, thermal

spraying techniques can be classified into methods such as plasma spraying, arc spraying, and high-velocity oxy-fuel (HVOF) spraying.<sup>91</sup> For the fabrication of MAX phase coatings, HVOF spraying is commonly employed. Frodelins *et al.*<sup>92</sup> utilized the HVOF spraying method to produce dense Ti<sub>2</sub>AlC coatings. In their experiments, the coatings, over 100 µm thick, exhibited good bonding with SS substrates and had a hardness ranging from 3–5 GPa. Nevertheless, the thermal spraying process necessitates the substrate to be heated to elevated temperatures, which constrains the choice of matrix materials and frequently results in the formation of cracks and potential delamination of the coating. Moreover, the thermal spraying process is prone to the formation of pores and metal oxides, resulting in a substantial presence of interfaces and defects within the coating. These issues negatively impact electron conduction within the coating, leading to poor electrical conductivity, as well as reduced heating efficiency and low utilization of the sprayed material. Thus, achieving large-scale production of MAX coatings through thermal spraying techniques still poses challenges.

Compared to thermal spraying, cold spraying technology utilizes high-speed and relatively low-temperature acceleration of micron-sized solid particles towards the substrate to form a coating through deformation and bonding mechanisms. Gutzmann *et al.*<sup>93</sup> achieved Ti<sub>2</sub>AlC coatings with a thickness of approximately 110–155 µm on Cu substrates using cold spraying. The coating maintained the crystalline structure of the starting material during the cold spraying process and exhibited a relatively low porosity. Maier *et al.*<sup>94</sup> utilized cold spraying to prepare Ti<sub>2</sub>AlC MAX phase coatings on Zr alloys. Experimental results demonstrated that the wear resistance of the coatings was significantly superior to that of the zirconium alloy substrate, with the depth of wear tracks reduced from 12 µm to 1 µm after coating deposition.

Cold spraying of MAX phase coatings avoids many issues such as tensile residual stress, low oxidation, adverse chemical reactions, and phase decomposition. However, cold spraying of MAX phase coatings typically requires micron-sized solid particles, and there are specific requirements for particle size and morphology. Additionally, the interface characteristics between cold-sprayed MAX phase coatings and the metal substrate are not yet well understood, including phenomena such as interface melting and interface amorphization.<sup>95</sup> Currently, only a few MAX phases, such as Ti<sub>3</sub>AlC<sub>2</sub>, Ti<sub>3</sub>SiC<sub>2</sub>, Cr<sub>2</sub>AlC, and Ti<sub>2</sub>AlC, have been studied and reported for cold-sprayed coatings.<sup>96</sup> To meet practical application demands, developing MAX phase coatings of different types is necessary. Although some studies have been conducted on the mechanical and wear properties of cold-sprayed MAX phase coatings, research on their high-temperature oxidation resistance, corrosion resistance, and electrical properties is still relatively limited. Further in-depth research is needed in these areas.

#### 2.4. Other methods

A new path for the production of MAX phase coating has been developed using a laser cladding layer, due to its advantages

such as high binding strength, low dilution rate, dense coating, good strength and toughness, and a small heat-affected zone. Richardson *et al.*<sup>97</sup> investigated the method of laser cladding for *in situ* synthesis and successfully prepared a three-layer dense and well-bonded Ti<sub>2</sub>AlC MAX phase composite coating with a thickness of  $1.33 \pm 0.02$  mm. It is the first instance of *in situ* synthesis of MAX phase coatings from elemental powders through laser cladding. Tian *et al.*<sup>98</sup> utilized a two-step approach of laser cladding and laser post-treatment to fabricate high-content Ti<sub>2</sub>AlC MAX phase coatings on a TC<sub>4</sub> titanium alloy substrate. During the laser cladding process, the diffusion of Al atoms resulted in the formation of a core-shell structure with TiC as the core and Ti<sub>2</sub>AlC as the shell in the coating. In the laser post-treatment process, the diffusion of C and Al atoms intensified, promoting the nucleation and growth of the Ti<sub>2</sub>AlC phase. Prior to laser post-treatment, the microhardness of the coating increased dramatically from the bonding region to the surface. After laser irradiation, with increasing laser power, the microhardness distribution in the coating became more uniform. This novel two-step laser technique opens up new prospects for the efficient fabrication of MAX phase coatings and related structures.

Electrophoretic deposition (EPD) is a method that involves suspending particles in a liquid medium and applying an electric field between two electrodes to uniformly coat the particles onto complex geometries. Galvin *et al.*<sup>99</sup> deposited Ti<sub>3</sub>SiC<sub>2</sub> coatings on titanium substrates through electrophoretic deposition and then performed rapid consolidation using laser sintering. By adjusting the laser power and focal length, they were able to achieve high coverage or good adhesion with approximately 30 µm thick coatings. This method is simple to operate, can be carried out at room temperature, and provides uniform coatings on complex geometries.

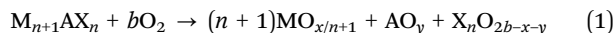
Zamulaeva *et al.*<sup>100</sup> prepared Cr<sub>2</sub>AlC coatings on Ti alloy substrates by applying pulsed electrical discharge. The results showed that the deposited coatings were primarily composed of the Cr<sub>2</sub>AlC phase, along with small amounts of γ-Al<sub>2</sub>O<sub>3</sub>, TiC, (Ti, Cr)C, and Cr<sub>1-x</sub>Al<sub>x</sub> phases. This technique allowed for the production of high-density coatings with good adhesion. However, the transient heating pulses and high heating and cooling rates during the pulsed electrical discharge process may result in overheating and thermal decomposition of the coating material, leading to the formation of impurity phases in the prepared coatings.

### 3. Protective performance of MAX phase coatings

#### 3.1. High temperature air oxidation resistance of MAX phase coatings

The formation of an Al<sub>2</sub>O<sub>3</sub> protective oxide coating plays an important role in the oxidation resistance of the material, which can greatly improve the service life of the material in the high-temperature air atmosphere.<sup>101</sup> In MAX phase coatings, due to the weaker M–A bond and stronger M–X bond, the Al element in

Al-containing MAX phase coatings readily diffuses to the surface and forms a dense, continuous passive coating, which exhibits excellent oxidation resistance under high temperature, and oxidation of the MAX phases occurs as follows:



In the present study, all oxidation kinetic curves of MAX-phase coatings exhibited parabolic shapes, which could be attributed to the initial rapid oxidation reaction of MAX phases upon exposure to oxygen. As the oxidation reaction progresses, a stable oxide layer formed on the surface of the MAX phase coating, effectively slowing down the oxidation process and establishing a protective layer. This results in a decrease in the rate of oxidation weight gain. Particularly noteworthy are the continuous and dense  $Al_2O_3$  coating produced during oxidation, which highlight the potential of  $Ti_2AlC$  and  $Cr_2AlC$  coatings as promising materials for high-temperature protection. Consequently, current research on the oxidation properties of MAX phase coatings has largely focused on Cr-based  $Cr_2AlC$  and Ti-based  $Ti_2AlC$  coatings.<sup>102–105</sup>

**3.1.1  $Cr_2AlC$  coating oxidation.** When exposed to high-temperature air,  $Cr_2AlC$  coatings can form oxide layers that reduce their oxidation rates. The formed  $Cr_2O_3$  and  $Al_2O_3$  oxide layers exhibit exceptional thermal and chemical stability, effectively preventing further oxidation of the  $Cr_2AlC$  coatings by oxygen or other oxidizing mediums. Mengis *et al.*<sup>106</sup> assessed the oxidation resistance of  $Cr_2AlC$  coatings in an air atmosphere at 800 °C over a period of 300 h. The results showed a lower mass gain in  $Cr_2AlC$  compared to the Ti4822 alloy substrate, with a very thin mixed oxide layer consisting of  $Cr_2O_3 + Al_2O_3$  forming on the coating surface. However, during the oxidation process, inward diffusion of Al and C elements occurred, leading to the decomposition of  $Cr_2AlC$  and the formation of binary compound phases such as  $Cr_7C_3$ ,  $Cr_{23}C_6$  and  $Cr_2Al$ , which reduced its high-temperature resistance. Li *et al.*<sup>107</sup> observed similar findings regarding the improved

oxidation resistance of  $Cr_2AlC$  coatings due to the formation of a continuous  $Al_2O_3$  coating at 900–1100 °C (Fig. 10). However, with increasing oxidation temperatures, the depletion of Al becomes more severe, resulting in the formation of  $Cr_7C_3$ . As a result of the inward diffusion of oxygen,  $Cr_7C_3$  undergoes oxidation, leading to the formation of an  $(Al, Cr)_2O_3$  solid solution oxide layer on the surface (Fig. 10b and d). Nonetheless, the presence of a large number of columnar crystals in  $Cr_2AlC$  coatings accelerates the inward diffusion of oxygen. Moreover, N in the air diffuses inward, reacting with Al to form  $AlN$  through columnar crystals, which increases the oxidation rate of  $Cr_2AlC$  coatings (Fig. 10b and c).

To improve the oxidation resistance of  $Cr_2AlC$  coatings, a diffusion barrier layer may be applied at the interface between the coating and substrate during the preparation process. Additionally, modifying the coating's columnar crystal structure to equiaxial crystals or reducing the number of columnar crystals can hinder oxygen diffusion pathways, ultimately leading to lower inward oxygen diffusion rates. These measures are believed to slow down inward oxygen diffusion and improve the oxidation resistance of  $Cr_2AlC$  coatings.

To inhibit internal nitridation and delay mutual diffusion rates at the coating/substrate interface, Li *et al.*<sup>108</sup> developed a three-layer  $Cr_2AlC$  coating structure, featuring a crystalline outer layer, an amorphous middle layer, and a  $(Cr, Al)_2O_3$  bottom layer. Compared to single-layer  $Cr_2AlC$  coatings, the three-layer structure demonstrated superior oxidation resistance at high temperatures, with lower oxidation weight gain observed. Nevertheless, multi-layer coating preparation can result in cracking during high-temperature oxidation, primarily due to significant thermal expansion coefficient mismatches and thermal stress concentration. To mitigate these factors, diffusion barrier layers can be incorporated between the coating and substrate to slow the mutual diffusion of coating elements and reduce Al consumption.

Wang *et al.*<sup>79</sup> conducted a study where they prepared MAX phase coatings on hastelloy substrates, consisting of Cr

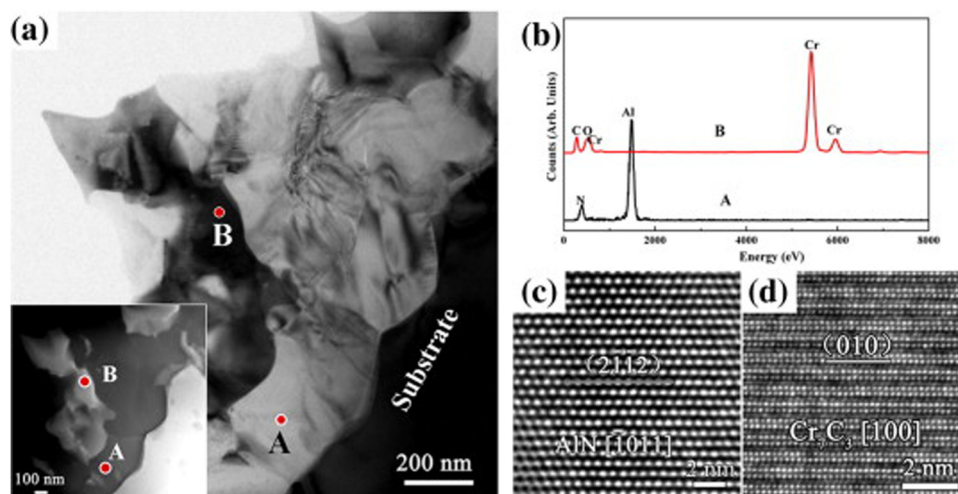


Fig. 10 (a) TEM bright-field image of the  $Cr_2AlC$  coating oxidized at 1000 °C for 20 h, where the inset shows the corresponding STEM image, (b) EDS profiles acquired from A and B points in (a), and (c) and (d) HRTEM images of points A and B in (a), respectively. Reproduced with permission.<sup>107</sup> Copyright 2011 Elsevier Ltd.



intermediate and Cr–Al–C layers (Fig. 11a). Following annealing at 700 °C for 5 h, the inward diffusion of coating elements resulted in the formation of a diffusion layer, transforming the Cr<sub>2</sub>AlC coating into an equiaxial crystal structure. As shown in Fig. 11b, after oxidation at 1000 °C for 40 h, a continuous Al<sub>2</sub>O<sub>3</sub> layer formed on the coating surface, with a Cr–C layer forming at the bottom. Upon increasing the oxidation temperature to 1100 °C, the oxide coating converted to (Al, Cr)<sub>2</sub>O<sub>3</sub>, and a Cr–C–N layer formed at the bottom due to nitridation. However, Al diffused inward and aggregated in the substrate, forming a continuous Al<sub>2</sub>O<sub>3</sub> layer. This Al<sub>2</sub>O<sub>3</sub> layer provided protection against further oxidation of the substrate and reduced elemental interdiffusion. It is notable, however, that Cr<sub>2</sub>AlC coatings exhibit limitations in oxidation resistance due to Al and Cr depletion and the generation of gases at high temperatures, which can lead to visible pore formation in the carbide layer.

Chen *et al.*<sup>109</sup> conducted a study comparing the high-temperature oxidation resistance of Cr<sub>2</sub>AlC coatings with columnar and equiaxial crystal structures (Fig. 12a and b). The equiaxial crystal Cr<sub>2</sub>AlC exhibited better oxidation resistance, characterized by a thinner oxide coating after oxidation. The grain boundaries of equiaxial crystals were denser than those of columnar crystals, reducing the diffusion rate of corrosive media. Intriguingly, nanopores (2–25 nm) were observed in the columnar grain boundaries, which reduced the oxidation resistance and increased the oxidation rate of Cr<sub>2</sub>AlC coatings. Therefore, reducing nanoporosity and transforming from columnar to equiaxed crystals can improve the oxidation resistance of Cr<sub>2</sub>AlC coatings.

Cr<sub>2</sub>AlC coatings have shown excellent oxidation resistance in high temperature atmospheres, and have also been widely

investigated in water vapor atmospheres. Tang *et al.*<sup>110</sup> investigated the water vapor oxidation behavior at 1000 °C of single layer Cr<sub>2</sub>AlC and Cr/Cr<sub>2</sub>AlC multilayer coatings for a short duration. The findings revealed that both coatings outperformed the Zr alloy substrate in terms of oxidation resistance, although their mass gain was similar. In the case of the Cr/Cr<sub>2</sub>AlC multilayer oxidation, the columnar grain boundaries of the Cr overlayer served as fast diffusion paths for the oxidation medium, resulting in internal oxidation beneath the Cr<sub>2</sub>AlC layer. Notably, oxidation occurred within both the Cr layer and the Cr<sub>2</sub>AlC layer, forming a protective Al<sub>2</sub>O<sub>3</sub> barrier that hindered the further inward diffusion of oxidizing species towards the substrate. Additionally, the high Cr content in the overlayer facilitated the formation of a passivation coating comprising Cr<sub>2</sub>O<sub>3</sub> at high temperatures. This dual-layer passivation coating (Cr<sub>2</sub>O<sub>3</sub>/Al<sub>2</sub>O<sub>3</sub>) effectively impeded the diffusion of corrosive media, making it a promising candidate for potential applications in accident-tolerant fuel (ATF) systems.

Wang *et al.*<sup>111</sup> fabricated a dense equiaxial crystal structure Cr<sub>2</sub>AlC MAX phase coating on a Zr alloy substrate, featuring a Cr/CrC<sub>x</sub> interfacial layer structure. The researchers investigated the steam oxidation resistance of the coating at temperatures ranging from 1000 to 1200 °C. The findings indicated that the incorporation of the interfacial layer played a significant role in inhibiting the rapid diffusion of Al into the substrate and preventing premature delamination of the coating during the annealing process. By selectively oxidizing Al, the coating experienced rapid growth of α-Al<sub>2</sub>O<sub>3</sub> on the surface while inhibiting the formation of other oxides. This enhanced the high-temperature steam oxidation capability of the Cr<sub>2</sub>AlC coating. However, the surface did not exhibit an (Al, Cr)<sub>2</sub>O<sub>3</sub>

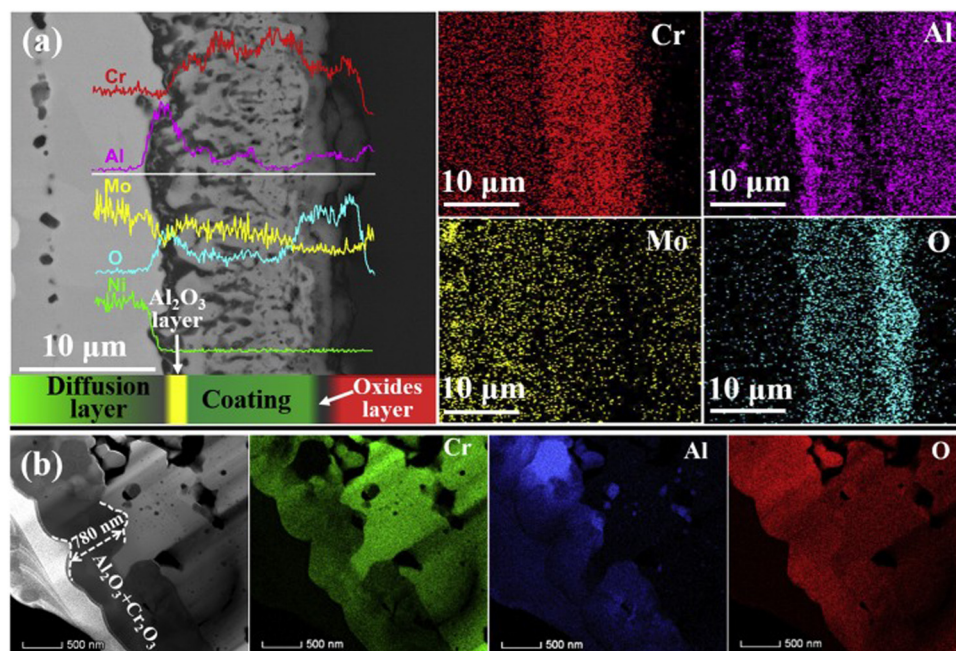


Fig. 11 (a) Cross-sectional image of the Cr<sub>2</sub>AlC coatings at 1000 °C for 40 h, and the corresponding line-scanning results. (b) Cross-sectional STEM micrographs of the outmost oxide layer for these oxidized Cr<sub>2</sub>AlC coatings. Reproduced with permission.<sup>79</sup> Copyright 2020 Elsevier Ltd.

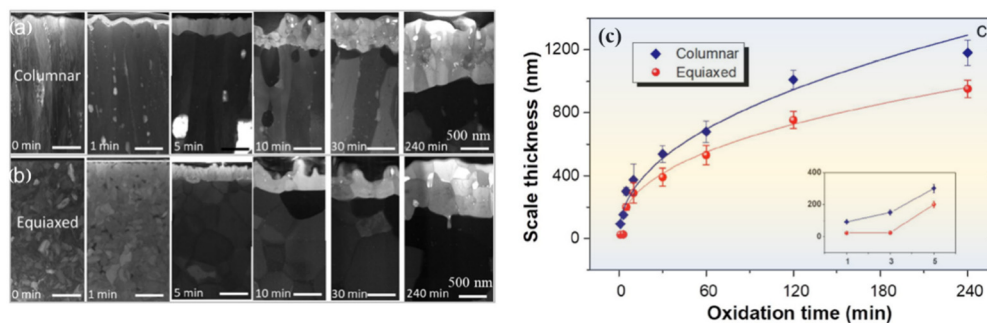


Fig. 12 STEM bright field images of the cross-sections of (a) columnar and (b) equiaxed grained  $\text{Cr}_2\text{AlC}$  coatings before oxidation and after oxidation at  $1100^\circ\text{C}$  from 1 to 240 min. (c) Variation of the oxide scale thickness with oxidation time and corresponding power lawfit in the equiaxed and columnar grained samples. Reproduced and adapted with permission.<sup>109</sup> Copyright 2020 Taylor & Francis INC.

coating, most likely due to the relatively short steam oxidation duration, leading to incomplete oxidation of the Cr element.

The aforementioned findings illustrate the exceptional oxidation resistance of  $\text{Cr}_2\text{AlC}$  coatings, which exhibit the ability to form passivation coatings of  $\text{Cr}_2\text{O}_3$  and  $\text{Al}_2\text{O}_3$  in high-temperature atmospheres. Nonetheless, it is important to note that at elevated temperatures, mutual diffusion occurs between the  $\text{Cr}_2\text{AlC}$  coatings and the substrate. This diffusion process, coupled with the depletion of Al content and the generation of gases, resulting in the formation of pore defects, thus reduced the service life of the coatings. Therefore, future research efforts should prioritize the structural design of the coatings, explore variations in crystal structure, investigate alterations in Al content, and delve into the dynamics of diffusion. These aspects represent key focal points for further exploration concerning the preparation and performance of  $\text{Cr}_2\text{AlC}$  coatings.

**3.1.2 Oxidation of  $\text{Ti}_2\text{AlC}$  coatings.**  $\text{Ti}_2\text{AlC}$  coatings exhibit excellent high temperature oxidation resistance and self-healing capabilities, primarily due to the formation of a continuous, dense  $\text{Al}_2\text{O}_3$  layer. Numerous studies have focused on  $\text{Ti}_2\text{AlC}$  coatings. Feng *et al.*<sup>112</sup> investigated the oxidation behavior of  $\text{Ti}_2\text{AlC}$  coatings at  $750^\circ\text{C}$ , compared to 316LSS substrates. The results showed that the oxide scale exhibited a distinct four-layer structure: the outermost layer comprised a mixed oxide layer of  $\text{TiO}_2$  and  $\text{Al}_2\text{O}_3$ , followed by a layer of  $(\text{Al}, \text{Cr})_2\text{O}_3$ , a mixed layer of  $\text{Fe}_2\text{O}_3$  and  $\text{TiO}_2$ , and the innermost layer consisting of  $\alpha\text{-Al}_2\text{O}_3$ . Notably, the presence of  $\text{Fe}_2\text{O}_3$  in the oxide layer indicated elemental mutual diffusion between the substrate and the coating. However, the  $\text{TiO}_2$  provided a diffusion pathway for oxygen within the outer mixed oxide layer. Consequently, the oxidation resistance of the  $\text{TiO}_2$  and  $\text{Al}_2\text{O}_3$  mixed oxide coating was less effective in inhibiting inward oxygen diffusion compared to a pure  $\text{Al}_2\text{O}_3$  coating. Additionally, the presence of  $\text{Fe}_2\text{O}_3$  created further diffusion channels, undermining the desired oxidation resistance and accelerating the oxidation process due to thermal expansion coefficient mismatches among the multiple oxides.

To inhibit mutual diffusion and improve adhesion between the coatings and substrate, Li *et al.*<sup>113</sup> prepared an intermediate layer of  $\text{TiC}$  between the  $\text{Ti}_2\text{AlC}$  coatings and investigated oxidation resistance at  $1000\text{--}1200^\circ\text{C}$ . The oxidation scale exhibits a three-layer structure, with the outermost layer being

a  $\text{TiO}_2 + \text{Al}_2\text{O}_3$  mixed oxide layer, the intermediate layer being  $\text{Al}_2\text{O}_3$ , and the inner layer being  $\text{TiO}_2$ . However, visible pore defects appeared, attributed to the diffusion of Ti following the Kirkendall mutual diffusion mechanism and the formation of  $\text{CO}_2$  and  $\text{H}_2$  during the reaction process.<sup>114</sup> The transformation of the oxide structure was closely related to the diffusion kinetics and thermodynamics of the elements in the M-site and A-site. Due to the fact that Al is bonded with weak bonds, outward diffusion more easily occurs during the oxidation process. However, because  $\text{TiO}_2$  has a more disordered structure than  $\text{Al}_2\text{O}_3$ , its growth rate is much higher than that of  $\text{Al}_2\text{O}_3$ . Thus, the outermost layer is a mixed oxide layer of  $\text{TiO}_2 + \text{Al}_2\text{O}_3$  at  $1000\text{--}1200^\circ\text{C}$ . As Al continues to diffuse and accumulate at the bottom of the outermost oxide layer, an  $\text{Al}_2\text{O}_3$  layer is formed. But as the Al in  $\text{Ti}_2\text{AlC}$  is depleted and aggregates in the middle layer,  $\text{TiC}$  forms, which is eventually fully oxidized to  $\text{TiO}_2$  due to the inward diffusion of oxygen.

Self-healing materials are capable of repairing cracks and damage automatically, thereby prolonging their service life. Wang *et al.*<sup>115</sup> achieved self-healing of cracks in  $\text{Ti}_2\text{AlC}$  coatings by Sn doping at  $700^\circ\text{C}$ . The primary mechanism for self-healing involved filling the cracks with  $\text{SnO}_2$  and  $\text{TiO}_2$ , which demonstrated better oxidation resistance than the unhealed coatings. However, achieving effective elemental doping requires consideration of factors such as the thermal expansion coefficient, thermal conductivity, and diffusion coefficient, all of which significantly affect the formation of cracks and other defects.<sup>116</sup> Meanwhile, the Al content also affects the formation of oxides.<sup>117</sup> The formation of a continuous, dense  $\text{Al}_2\text{O}_3$  layer consumes a large amount of Al in the coating. Insufficient Al content can hinder the formation of  $\text{Al}_2\text{O}_3$  during oxidation and lead to the formation of  $\text{TiO}_2$  in the outer oxide layer, which is detrimental to the oxidation resistance of  $\text{Ti}_2\text{AlC}$  coatings at high temperatures.

### 3.2. Corrosion of MAX phase coatings in harsh environments

**3.2.1 Salt spray corrosion of MAX phase coatings.** MAX phase coatings exhibit excellent protective performance by effectively blocking the diffusion pathways of corrosive and oxidizing media under high-temperature oxidation conditions due to the formation of a continuous and dense oxide layer on their surfaces.<sup>118</sup> However, in specific corrosive environments,

such as those containing NaCl, the surface oxide layer is severely damaged, resulting in the formation of numerous porous salt-metal-oxide complex compounds. This disrupts the dense and continuous oxide coating on the surface and poses greater challenges compared to oxidizing environments. Nonetheless, MAX phase coatings possess strong corrosion resistance due to the unique structure, which enables the easy formation of oxide coatings and certain self-healing capabilities.<sup>119</sup>

To explore the corrosion mechanism of  $\text{Ti}_2\text{AlC}$  MAX phase coatings in NaCl solution, Fu *et al.*<sup>120</sup> compared the corrosion resistance of the amorphous Ti–Al–C coatings and  $\text{Ti}_2\text{AlC}$  coatings in a 3.5 wt% NaCl aqueous solution. The  $\text{Ti}_2\text{AlC}$  coatings exhibited a higher corrosion potential value ( $-0.301$  V) and a lower corrosion current density value ( $5.82 \times 10^{-8} \text{ A cm}^{-2}$ ) compared to those of amorphous coatings ( $-0.618$  V and  $1.44 \times 10^{-6} \text{ A cm}^{-2}$ ). The exceptional corrosion resistance of  $\text{Ti}_2\text{AlC}$  coating was attributed to the high mobility of active Al atoms, which could readily migrate to the coating surface and form a dense  $\text{Al}_2\text{O}_3$  oxide layer. This  $\text{Al}_2\text{O}_3$  layer acts as a passivation barrier, effectively preventing further corrosion during chemical attacks.

Wang *et al.*<sup>49</sup> conducted a comprehensive investigation on the corrosion process of  $\text{Ti}_2\text{AlC}$  MAX phase coatings in NaCl deposits in water vapor at  $600^\circ\text{C}$ . After subjecting the  $\text{Ti}_2\text{AlC}$  coatings to 75 h of corrosion, a compact and continuous corrosion scale with a thickness of  $3 \mu\text{m}$  was observed on the coating surface, leading to remarkable corrosion resistance. This dense corrosion scale was composed of  $\text{Na}_x\text{Ti}_y\text{O}_z$  fine grains with a size of  $11 \pm 0.4 \text{ nm}$  and amorphous  $\text{Al}_2\text{O}_3$  phases, which self-healed the generated defects during corrosion, benefiting from the novel layered structure of the MAX phase.

Li *et al.*<sup>121</sup> conducted a comparative study on the hot NaCl salt corrosion behavior of three kinds of MAX phase materials

( $\text{Ti}_3\text{SiC}_2$ ,  $\text{Ti}_2\text{AlC}$  and  $\text{Cr}_2\text{AlC}$ ) at a high temperature of  $750^\circ\text{C}$  for 240 h. They found that  $\text{Ti}_3\text{SiC}_2$  exhibited the best high-temperature corrosion resistance, maintaining its surface integrity well after corrosion (Fig. 13a), without layering phenomenon in the corrosion layer (Fig. 13d). The surface damage of  $\text{Ti}_2\text{AlC}$  after corrosion was more significant (Fig. 13b), and its corrosion products mainly consisted of rod-shaped  $\text{TiO}_2$ , bright block shaped  $\text{Al}_2\text{O}_3$ , and the presence of  $\text{Na}^+$  in its oxide layer (Fig. 13e). However,  $\text{Cr}_2\text{AlC}$  exhibited the worst high-temperature corrosion resistance (Fig. 13c). The generated oxide layer had a three-layer structure: the upper layer was  $\text{Al}_2\text{O}_3$ , the middle layer was  $\text{Cr}_2\text{O}_3$ , and the lower layer was  $\text{Cr}_7\text{C}_3$  (Fig. 13f). Its poor high-temperature corrosion resistance was primarily due to its strong reaction with NaCl, which produces volatile  $\text{Na}_2\text{CrO}_4$ , making it difficult to form a dense oxide layer on the surface of  $\text{Cr}_2\text{AlC}$ .

**3.2.2 Corrosion of MAX phase coatings in NaCl solution.** Li *et al.*<sup>122</sup> studied the electrochemical performance of  $\text{Ti}_2\text{AlC}$  MAX phase coatings in a 3.5 wt% NaCl solution and found that high-purity  $\text{Ti}_2\text{AlC}$  MAX phase coatings exhibited significantly enhanced impedance characteristics and lower corrosion current density. The excellent corrosion resistance is attributed to the high transport kinetics of Al atoms in the  $\text{Ti}_2\text{AlC}$  coating, which is conducive to the preferential formation of the  $\text{Al}_2\text{O}_3$  passivation layer (Fig. 14a). Moreover, over 50% of Al vacancies have a high tolerance, providing favorable conditions for the formation of stable defect-type  $\text{Ti}_2\text{Al}_x\text{C}$  structures after consuming Al elements. Zhu *et al.*<sup>123</sup> investigated the corrosion behavior of  $\text{Ti}_3\text{SiC}_2$  and  $\text{Ti}_3\text{AlC}_2$  in a 3.5% NaCl solution. Compared to Ti substrates, both  $\text{Ti}_3\text{SiC}_2$  and  $\text{Ti}_3\text{AlC}_2$  coatings demonstrated markedly enhanced passivation properties. This superiority is attributed to the distinctive layered structure of the MAX phase, which promotes the diffusion of A-site Si/Al atoms.

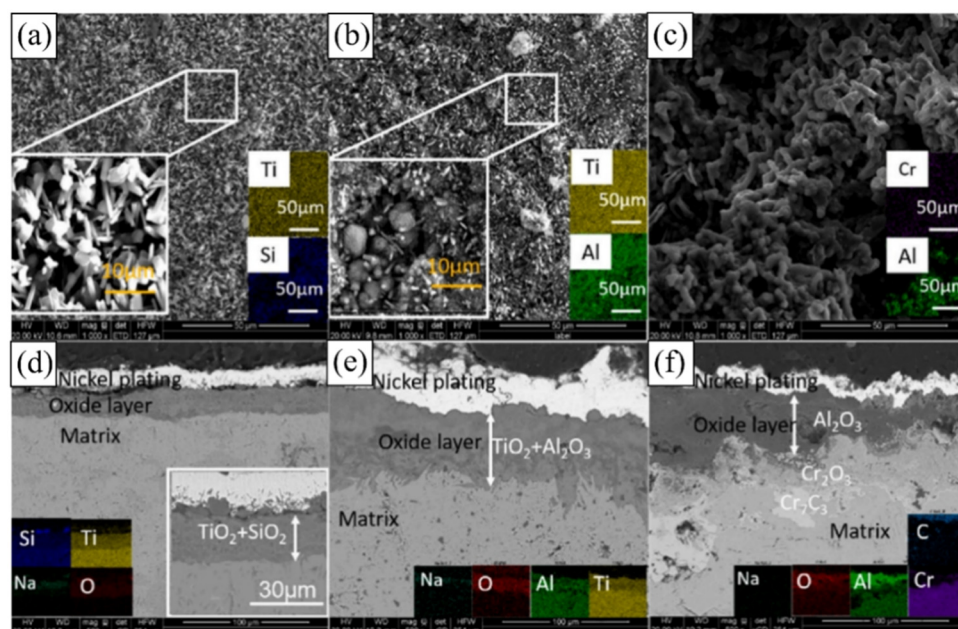


**Fig. 13** Surface and cross-sectional morphology after corrosion: (a)–(c) are the surface morphology and (d)–(f) are the cross-sectional morphology of  $\text{Ti}_3\text{SiC}_2$ ,  $\text{Ti}_2\text{AlC}$ , and  $\text{Cr}_2\text{AlC}$ . Reproduced with permission.<sup>121</sup> Copyright 2022 Elsevier Ltd and Techna Group S.r.l.



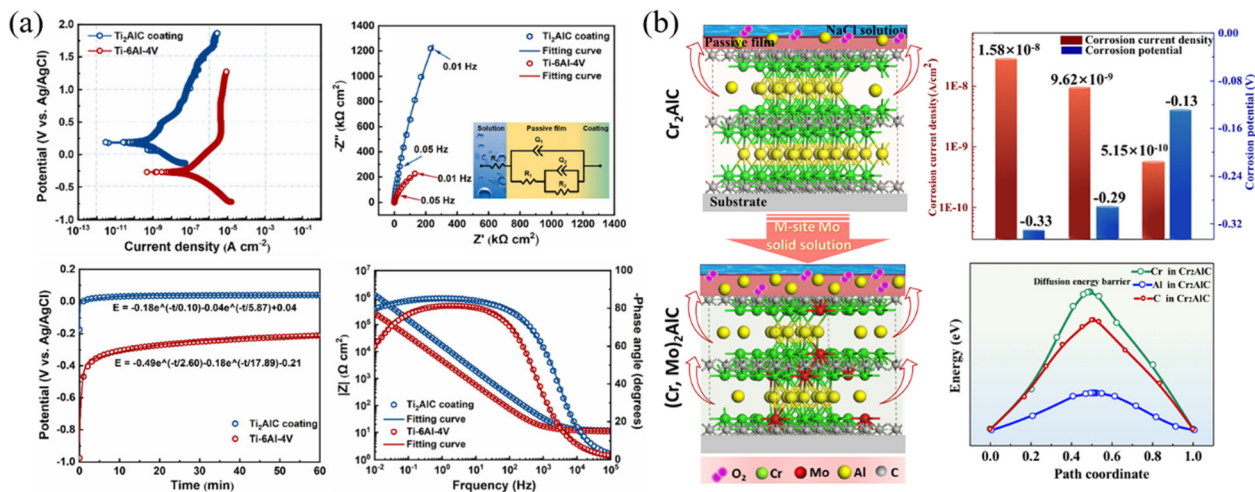


Fig. 14 (a) Electrochemical performance of the Ti<sub>2</sub>AlC coating and uncoated Ti-4Al-4V in 3.5 wt% NaCl solution. (b) Schematic of the mechanism and electrochemical performance for the comparative corrosion inhibition of Cr<sub>2</sub>AlC MAX phase coating with and without an Mo solid solution in 3.5 wt% NaCl solution. Reproduced and adapted with permission.<sup>122,124</sup> Copyright 2024 Elsevier Ltd and 2024 American Chemical Society.

As a consequence, the atomic passivation efficiency is observed to be lower when these atoms diffuse to the barrier layer, thereby contributing to the improved passivation characteristics of these coatings. Additionally, Ti<sub>3</sub>SiC<sub>2</sub> has better corrosion resistance due to its Si layer being more stable than the Al layer in Ti<sub>3</sub>AlC<sub>2</sub>.

Recently, Zhang *et al.*<sup>125</sup> studied the corrosion behavior of the amorphous, partially crystalline, and fully crystalline Cr<sub>2</sub>AlC MAX phase coatings in 3.5 wt% NaCl aqueous solutions. It was revealed that both Cr and Al played important roles in the corrosion process. To further increase the electrochemical corrosion resistance, Zhang and co-authors<sup>124</sup> fabricated (Cr<sub>0.9</sub>, Mo<sub>0.1</sub>)<sub>2</sub>AlC coatings based on the concept of M-site solid solutions. Results showed that the corrosion current density of (Cr, Mo)<sub>2</sub>AlC solid solutions was reduced, and the electric impedance was enhanced by about an order of magnitude in 3.5 wt% NaCl solution compared to pristine Cr<sub>2</sub>AlC coating. According to the density functional theory (DFT) simulation, this phenomenon was mainly ascribed to the partial substitution of Mo for Cr in Cr<sub>2</sub>AlC, which favored the stronger mobility of Al atoms due to the reduction in vacancy formation energy, leading to the rapid growth of passivating Al oxides substantially (Fig. 14b).

**3.2.3 Corrosion of MAX phase coatings under other harsh environments.** Shi *et al.*<sup>126</sup> conducted an in-depth comparative study on the corrosion behavior of Al-containing MAX phase coatings in 10<sup>-6</sup> wt% oxygen-containing molten Pb for 3200 h at 600 °C. Three distinct MAX-phase coatings (Cr<sub>2</sub>AlC, Ti<sub>2</sub>AlC and Ti<sub>3</sub>AlC<sub>2</sub>) demonstrated corrosion resistance against molten Pb through the formation of a protective oxide layer. Specifically, the Cr<sub>2</sub>AlC coating developed an Al<sub>2</sub>O<sub>3</sub> scale with a small amount of Cr<sub>2</sub>O<sub>3</sub>. In contrast, both the Ti<sub>2</sub>AlC and Ti<sub>3</sub>AlC<sub>2</sub> coatings displayed a mixed Al<sub>2</sub>O<sub>3</sub> and TiO<sub>2</sub> oxide scale. However, a more complex mixed oxide layer consisting of VO<sub>2</sub>, V<sub>4</sub>O<sub>7</sub>, and Pb<sub>3</sub>(VO<sub>4</sub>)<sub>2</sub> phases formed on the V<sub>2</sub>AlC coating, leading to the complete consumption of the MAX-phase coating.

Zakeri-Shahroudi *et al.*<sup>127</sup> investigated the performance of Cr<sub>2</sub>AlC MAX phase coatings in the presence of 40 wt% V<sub>2</sub>O<sub>5</sub> + 60 wt% Na<sub>2</sub>SO<sub>4</sub>. After 5 h of cyclic hot corrosion behavior at 900 °C, it was found that the Cr<sub>2</sub>AlC coating exhibited good corrosion resistance for up to 30 h. But, after 40 h, microcracks appeared on the sample surface. With the corrosion time increased to 50 h, the sample was completely degraded due to spallation.

### 3.3. Mechanical performance protection of MAX phase coatings

Due to the unique nano-laminated structure and combination of covalent, ionic and metallic chemical bonds, MAX phases generally exhibit high stiffness, compressive strength, and fracture toughness.<sup>128</sup> According to the well-known Hall-Petch relationship, MAX phase coatings are expected to be stronger and harder than their corresponding bulk materials because the grains in coatings are typically smaller than those in bulk materials. Table 1 summarizes the hardness and modulus of common MAX phases such as Cr<sub>2</sub>AlC, Ti<sub>2</sub>AlC, Ti<sub>3</sub>AlC<sub>2</sub> and Ti<sub>3</sub>SiC<sub>2</sub>. Most MAX phase coatings exhibit a hardness of 10–20 GPa and a modulus of 200–300 GPa, which impart greater resistance to impact and wear, making them promising for applications as protective coatings.

Preparation parameters and methods are widely investigated to improve the mechanical properties of MAX phase coatings. Naveed *et al.*<sup>129</sup> deposited Cr<sub>2</sub>AlC coatings with different sputtering powers, resulting in variations in the inter-metallic AlCr<sub>2</sub> and Cr<sub>7</sub>C<sub>3</sub> carbide phases and the preferred orientation of the coating. Hardness values were measured in the range of 11–14 GPa, showing a slight increase with increasing sputtering powers, which was attributed to the preferred orientation. Du *et al.*<sup>130</sup> studied the temperature effect on the bulk moduli of Cr<sub>2</sub>AlC within the quasiharmonic Debye model by first-principles GGA+U calculations, which

**Table 1** Summary of the hardness of Cr<sub>2</sub>AlC, Ti<sub>2</sub>AlC, Ti<sub>3</sub>AlC<sub>2</sub>, Ti<sub>3</sub>SiC<sub>2</sub> and V<sub>2</sub>AlC coatings

Coatings	Hardness (GPa)	Modulus (GPa)	Ref.
Cr <sub>2</sub> AlC	13.7 ± 0.5	196 ± 14	<i>Wear</i> , 2018, <b>402–403</b> , 187–195
	19.0 ± 1.7	268 ± 16	<i>J. Alloys Compd.</i> , 2018, <b>753</b> , 11–17
	13 ± 2	298 ± 21	<i>Scr. Mater.</i> , 2007, <b>57</b> , 1137–1140
	16 ± 2	—	<i>Mater. Design</i> , 2021, <b>206</b> , 109757
	16.6 ± 0.5	261 ± 7	<i>Mater. Des.</i> , 2022, <b>222</b> , 111060
	12.8 ± 0.4	334 ± 24	<i>J. Mater. Sci. Technol.</i> , 2023, <b>143</b> , 140–152
	18.4 ± 0.8	328 ± 26	<i>Wear</i> , 2024, <b>540–541</b> , 205221
	15.4	288	<i>Surf. Coatings Technol.</i> , 2013, <b>235</b> , 454–460
	15.1 ± 1.8	259 ± 20	<i>J. Nucl. Mater.</i> , 2019, <b>526</b> , 151742
	15.3 ± 3.6	254 ± 22	<i>Intermetallics</i> , 2023, <b>163</b> , 108039
Ti <sub>2</sub> AlC	11.6 ± 0.3	—	<i>Adv. Eng. Mater.</i> , 2022, <b>24</b> , 1–11
	11.2 ± 1.4	191 ± 26	<i>Wear</i> , 2015, <b>342–343</b> , 391–397
	17.2 ± 1.6	257 ± 12	<i>Surf. Coatings Technol.</i> , 2017, <b>309</b> , 445–455
	15.8 ± 2.1	273 ± 20	<i>Surf. Coatings Technol.</i> , 2018, <b>334</b> , 384–393
	17.9 ± 0.8	279 ± 4	<i>J. Eur. Ceram. Soc.</i> , 2023, <b>43</b> , 4673–4683
	10.2 ± 0.5	221 ± 10	<i>Appl. Surf. Sci.</i> , 2021, <b>537</b> , 147864
	16.9 ± 0.5	347 ± 16	<i>J. Mater. Sci. Technol.</i> , 2023, <b>143</b> , 140–152
	14.2 ± 0.1	231 ± 3	<i>Ceram. Int.</i> , 2019, <b>45</b> , 13912–13922
Ti <sub>3</sub> AlC <sub>2</sub>	3.2 ± 0.8	120 ± 21	<i>Appl. Surf. Sci.</i> , 2021, <b>537</b> , 147864
	5.3 ± 0.9	—	<i>Adv. Eng. Mater.</i> , 2022, <b>24</b> , 1–11
	12.3 ± 1.1	232 ± 11	<i>J. Eur. Ceram. Soc.</i> , 2023, <b>43</b> , 4673–4683
	19 ± 1	250 ± 9	<i>Appl. Phys. Lett.</i> , 2004, <b>85</b> , 1066–1068
	20.7 ± 0.5	237 ± 4	<i>J. Eur. Ceram. Soc.</i> , 2022, <b>42</b> , 2073–2083
Ti <sub>3</sub> SiC <sub>2</sub>	18.0	240 ± 4	<i>Mater. Charact.</i> , 2022, <b>194</b> , 112421
	19 ± 1	282 ± 9	<i>J. Appl. Phys.</i> , 2004, <b>96</b> , 4817–4826
	11.1 ± 1.6	229 ± 4	<i>Mater. Sci. Technol.</i> , 2013, <b>29</b> , 975–979

revealed the origin of the deviation between the experimental and theoretical data.

Eichner *et al.*<sup>131</sup> confirmed that the hardness of the Cr<sub>2</sub>AlC coating on softer IN718 substrates with a (100) preferred orientation was higher than the hardness measured in cross-sections. Yang *et al.*<sup>40</sup> studied the elastic anisotropies, thermodynamic and tensile properties of Ti<sub>2</sub>AX (A = Al and Ga, X = C and N) MAX phases using first-principles calculations. The calculated anisotropy indexes indicated that the MAX phases were anisotropic in elastic modulus. Moreover, according to the tensile calculation, the tensile strength along the [110] direction is greater than that along the [001] direction, and fracture failure will occur in the [110] direction. Li *et al.*<sup>132</sup> predicted the mechanical and thermodynamics of MAX phase V<sub>2</sub>SiC under different pressures based on DFT simulations. The results showed that elastic constants satisfied the Born stability criterion, ensuring mechanical stability under pressurized and unpressurized conditions. And the increase in *U* from 0.239 to 0.279 indicated that the compound changed from brittle to ductile, with the maximum ductility observed at 20 GPa. Liu *et al.*<sup>133</sup> compared the mechanical properties of different phase compositions in Cr<sub>2</sub>AlC coatings obtained by varying the current of the Al target during the deposition process. When the Al content was maximized at an Al-target current of 1.0 A, the coating exhibited the highest hardness, elastic modulus, *H/E*, *H<sup>2</sup>/E<sup>2</sup>* and toughness fracture. Increasing or decreasing the Al-target current led to a reduction in Cr<sub>2</sub>AlC content and an increase in intermetallic Al<sub>8</sub>Cr<sub>5</sub>, which deteriorated the hardness and fracture toughness of the coatings. This phenomenon demonstrates that reducing ductile intermetallic content in MAX phase coatings is in favor of their mechanical properties.

Rueß *et al.*<sup>134</sup> investigated the mechanical properties of Cr<sub>2</sub>AlC prepared by DCMS and HiPIMS, respectively. Generally, the coating prepared by HiPIMS had superior density and larger elastic moduli compared to that prepared by DCMS, indicating that ion bombardment by ionized coating-forming species is beneficial. The findings demonstrated that there is an optimum ion energy for forming dense and high-purity MAX phase coatings. Too low energy results in the formation of under-dense coatings, while too high energy yields the formation of (Cr, Al)<sub>2</sub>C<sub>x</sub> in addition to Cr<sub>2</sub>AlC. Similar observations were reported by Völker *et al.*<sup>135</sup> and Qureshi *et al.*,<sup>71</sup> where the hardness and modulus of Cr<sub>2</sub>AlC coatings prepared by HiPIMS were higher than those prepared by DCMS. The HiPIMS-deposited coating had the highest fracture toughness 2.0 ± 0.2 MPa m<sup>1/2</sup>, whereas the coating deposited by DCMS had the lowest value of 1.8 ± 0.1 MPa m<sup>1/2</sup>.<sup>135</sup> This further explains the influence of preparation methods on the fracture toughness of Cr<sub>2</sub>AlC coatings. The equiaxed crystal coating prepared by HiPIMS has entangled grain boundaries and a longer crack propagation path compared to the columnar crystal coating deposited by DCMS, demonstrating better crack resistance.

Molina-Aldareguia *et al.*<sup>136</sup> analyzed the deformation mechanisms in single-crystal Ti<sub>3</sub>SiC<sub>2</sub> (0001) coatings by nanoindentation. Basal plane dislocation glide created dislocation walls and formed kink bands and delamination cracks at the free surface near indentations. Yuan *et al.*<sup>137</sup> studied the mechanical properties of Cr<sub>2</sub>AlC coatings with a grain size of 88 nm by nanoindentation. An ultrahigh compressive strength of 5.3 GPa and plastic strain beyond 12.5% were achieved in the Cr<sub>2</sub>AlC coating according to micropillar compression tests

(Fig. 15a). Several slip bands at  $45^\circ$  from the load direction were visible in the compressed micropillar without vertical cracks or delamination (Fig. 15b). TEM micrographs of the deformed region revealed the synchronous emergence of two dislocations under the diffraction vector  $g = 0001$ , demonstrating that these were not routine basal dislocations with Burger's vector  $b = 1/3\langle 11\bar{2}0 \rangle$  (Fig. 15c and d). These non-basal dislocations form in nanograins under complex stress states, thereby increasing the forms of dislocation slip and ultimately enhancing the plasticity deformation ability. Additionally, deformation twins were observed in the severely-deformed region (Fig. 15e). SAED patterns (Fig. 15f) displayed close but distinctly separate spots ( $10\bar{1}3$ ) shared by the matrix and twin, confirming the presence of an incoherent ( $10\bar{1}3$ ) twin boundary. These twins, which withstand high shear stress during deformation, favor the enhancement of both strength and plasticity.

For MAX phase coatings prepared by the deposition-annealing two-step method, the annealing process plays a crucial role in determining the mechanical properties of the coatings. In general, the preparation requires a specific annealing temperature range. As the annealing temperature increases, the hardness of the coating typically increases because as-deposited coatings are often amorphous or partially crystalline with low hardness, and heating transforms this disordered structure into densely arranged hexagonal layered MAX phases.<sup>138–140</sup> However, further increases in annealing temperature can lead to either a decrease or an increase in hardness. The former is due to grain growth at elevated temperature, while the latter is associated with phase transitions, such as the formation of the hard TiC phase resulting from the decomposition of  $\text{Ti}_3\text{AlC}_2$  and  $\text{Ti}_2\text{AlC}$  coatings above  $900^\circ\text{C}$ .<sup>59,141</sup>

Zhang *et al.*<sup>142</sup> found that the porosity of  $\text{Ti}_3\text{SiC}_2$  coatings significantly declined with the increasing annealing temperature at  $500\text{--}900^\circ\text{C}$ , contributing to gradually improved hardness and fracture toughness of the coating. Wang *et al.*<sup>143</sup> investigated the annealing effect on the helium-irradiated  $\text{Cr}_2\text{AlC}$  coating. As the annealing temperature increased, the gradual recovery in the hardness of the MAX phase coating was observed due to the recombination of defects, suggesting that appropriately raising the annealing temperature could enhance the mechanical properties of MAX phase coatings by eliminating defects.

Moreover, alloying to form solid solution is an effective method to improve the mechanical properties of MAX phase coatings.<sup>144–146</sup>  $\text{Cr}_2\text{AlC}$  MAX phase coatings typically suffer from low hardness and toughness as well as a lack of lubrication at high temperature. Wang *et al.*<sup>147</sup> demonstrated that the hardness of the  $\text{Cr}_2\text{AlC}$  MAX phase coating was enhanced by 34.3% when Cr was partially substituted with V (47 at%), and the coating toughness was also improved (Fig. 16a). Simultaneously, both the friction coefficient and the wear rate of the coatings at  $900^\circ\text{C}$  against  $\text{Al}_2\text{O}_3$  balls were significantly reduced at 47 at% V (Fig. 16b), which was attributed to the formation of a large number of molten  $\text{V}_2\text{O}_5$  that encapsulated (Cr, Al) $_2\text{O}_3$  hard crystal grains (Fig. 16c).

## 4. New functional protection performance of MAX phase coatings

### 4.1. Protection on metal bipolar plates

MAX phase materials, with their unique crystal structure, combine the excellent electrical and thermal conductivity of

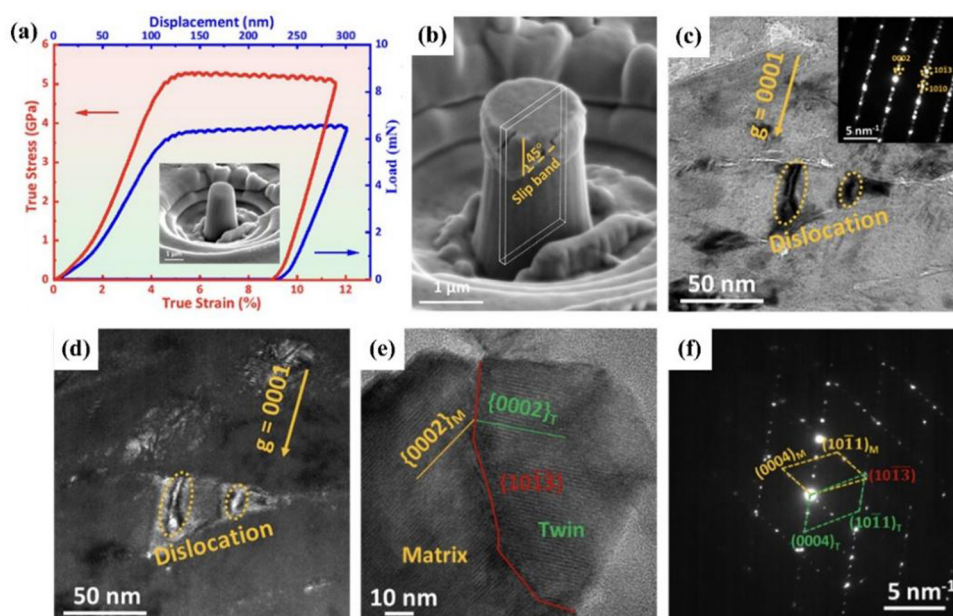


**Fig. 15** Micropillar compression test of  $\text{Cr}_2\text{AlC}$  coatings: (a) load–displacement and true stress–strain curves of the  $\text{Cr}_2\text{AlC}$  coating micropillar. (b) SEM image of the micropillar after compression. (c) Bright-field TEM micrograph of a deformed grain under the diffraction vector  $g = 0001$ . (d) Weak-beam dark-field micrograph of (c). (e) HRTEM micrograph of the twins in the deformed region. (f) SAED patterns in (e). Reproduced with permission.<sup>137</sup> Copyright 2023 Acta Materialia Inc, Elsevier Ltd.



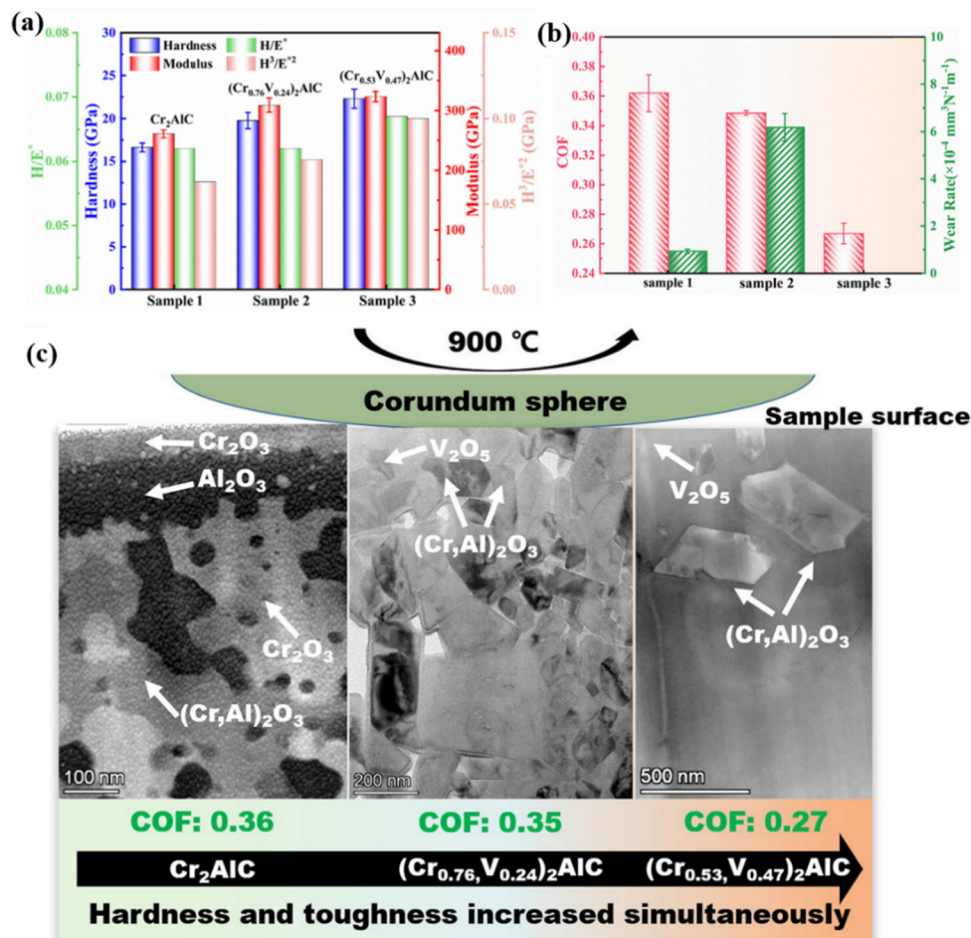


Fig. 16 Characterization of  $(\text{Cr}_{1-x}\text{V}_x)_2\text{AlC}$  coatings: (a) hardness, elastic modulus,  $H/E$  and  $H^3/E^2$  of the coatings obtained by nanoindentation. (b) COF and wear rate. (c) Schematic diagram of the friction mechanism. Reproduced with permission.<sup>147</sup> Copyright 2022 Elsevier Ltd.

metals and the high-temperature oxidation resistance and corrosion resistance of ceramics. This makes them an ideal protective coating material for metal bipolar plates in proton exchange membrane fuel cells (PEMFCs).<sup>148</sup> Abbas *et al.*<sup>64</sup> applied  $\text{Ti}_2\text{AlC}$  MAX phase coating to metal bipolar plates for testing. Due to the formation of the  $\text{Ti}_2\text{AlC}$  MAX phase, the coating exhibited excellent electrical conductivity, with an interfacial contact resistance (ICR) of only  $3.27 \text{ m}\Omega \text{ cm}^2$ , much lower than the United States Department of Energy (DOE) standard.<sup>149</sup> Lu *et al.*<sup>58</sup> studied the conductive and corrosion-resistant protective performance of  $\text{Ti}_3\text{AlC}_2$  MAX phase coating on SS304 with a TiC diffusion layer in  $\text{H}_2\text{SO}_4$  solution (pH = 3) containing 2 ppm  $\text{F}^-$  at  $70^\circ\text{C}$  in simulated PEMFC environments. The ICR of the  $\text{Ti}_3\text{AlC}_2$ -coated SS304 was only  $3.725 \text{ m}\Omega \text{ cm}^2$  at  $140 \text{ N cm}^{-2}$ . The outstanding electrical conductivity was attributed to the presence of an easier pathway for the transport of electrons *via*  $\text{Ti}_3\text{AlC}_2$  channels. In the potentiostatic polarization test simulating PEMFC environments, the average current densities at  $0.6 \text{ V}$  (vs. SCE) and  $-0.1 \text{ V}$  (vs. SCE) were  $8.0 \times 10^{-7} \text{ A cm}^{-2}$  and  $5.0 \times 10^{-8} \text{ A cm}^{-2}$ , respectively, demonstrating the coating's excellent corrosion resistance and durability. Moreover, Lu, *et al.*<sup>57</sup> also studied the protection performance of  $\text{Ti}_3\text{SiC}_2$  on metal bipolar plates.

Ma *et al.*<sup>77</sup> studied the conductivity and corrosion resistance of MAX phase coatings with different degrees of crystallization. The as-deposited samples showed the best corrosion resistance, with a stable potentiostatic polarization current density of  $3.7 \times 10^{-7} \text{ A cm}^{-2}$ , much lower than the corrosion current density of the SS316L substrate. This improvement was attributed to the preferential formation of the passivation film on the surface of amorphous coatings. The strength of corrosion resistance is ascribed to the differences in passivation films, which can be traced back to the differences in the stacking of atoms with different orientations in the crystal. Subsequently, they fabricated  $\text{Cr}_2\text{AlC}$  coatings with different crystallographic orientations on SS316L.<sup>79</sup> The  $\text{Cr}_2\text{AlC}$  coating with a (103) preferred orientation exhibited the best corrosion resistance, with an average current density of  $9.0 \times 10^{-3} \mu\text{A cm}^{-2}$ , because the exposed Cr atom in coatings with (103) preferred orientation had the lowest binding energy and was more likely to preferentially form a passivation film by binding with oxygen. Liu *et al.*<sup>150</sup> also researched the conductivity and corrosion resistance of  $\text{Cr}_2\text{AlC}$  MAX phase coating, finding that the corrosion current of the coated sample was  $2.43 \times 10^{-7} \text{ A cm}^{-2}$ , two orders of magnitude lower than that of the uncoated SS304.

#### 4.2. Radiation resistance property

MAX phases have emerged as a promising structural material for components requiring high-temperature durability and exposure to extreme radiation environments in upcoming nuclear reactors.<sup>151–155</sup> Neutron or ion radiation exposure can induce the accumulation of Frenkel defects, such as voids and interstitial atoms, due to displacement cascades within materials.<sup>154,156</sup> Assessing the radiation resilience of MAX phases is essential to identify the most suitable MAX phases for this domain.<sup>157–159</sup> Bowden *et al.*<sup>160</sup> assessed the radiation resilience of MAX phase coatings of  $\text{Zr}_3\text{AlC}_2$ ,  $\text{Nb}_4\text{AlC}_3$ , and  $(\text{Zr}_{0.5}, \text{Ti}_{0.5})_3\text{AlC}_2$  by proton irradiation followed by post-irradiation examination based primarily on X-ray diffraction analysis. The findings indicated that Zr-based 312-MAX phase,  $\text{Zr}_3\text{AlC}_2$  and  $(\text{Zr}_{0.5}, \text{Ti}_{0.5})_3\text{AlC}_2$ , exhibited remarkable defect recovery capabilities above 400 °C, whereas  $\text{Nb}_4\text{AlC}_3$  showed no significant defect recovery below 600 °C. DFT calculations suggest that the structural distinctions between the 312 and 413 MAX phases govern the variations in radiation resistance observed in these materials. Similarly, Dai *et al.*<sup>161</sup> and Duan *et al.*<sup>162</sup> investigated the point defect and mono-vacancy defective in the MAX phase  $\text{Cr}_2\text{AlC}$  coating using first-principles calculations, which suggested the excellent anti-radiation performance in nuclear applications.

#### 4.3. Electromagnetic shielding performance

In recent years, there has been significant focus on the MAX phase coatings as exceptional electromagnetic interference (EMI) shielding materials due to their high conductivity, remarkable thermal conductivity, resistance to high temperatures and oxidation resistance.<sup>163–165</sup> The superior EMI shielding capabilities of MAX phases stem from their high absorption and reflection of EM waves. Huang and co-authors<sup>166</sup> studied the EMI shielding performance of MAX@ carbonised wood (CW) composites ( $\text{Ti}_2\text{AlC@CW}$ ,  $\text{V}_2\text{AlC@CW}$  and  $\text{Cr}_2\text{AlC@CW}$ ) with a porous structure. The MAX@CW composite materials preserve the porous structure characteristics of CW templates, while the CW template facilitates the oriented assembly of the MAX phase by filling the porous structure of CW, creating multiple interfaces. These distinctive structures establish a pathway for terahertz wave dissipation in porous network structures, leading to a notable rise in transmission loss. Consequently, MAX@CW composite materials display significantly higher shielding effectiveness than CW.

#### 4.4. MAX phase as a bond coating for thermal barrier coatings

In order to prevent the interdiffusion of elements at the substrate alloy/coating interface, MAX phase coatings are also used as intermediate or diffusion barriers in some composites.<sup>167,168</sup> For example, Li *et al.*<sup>105,169</sup> assesses the performance of  $\text{Cr}_2\text{AlC}$  coatings as a thin transition layer between the  $\text{NiCrAlY}$  coating and alloy substrate at high temperature. It was observed that the Al in  $\text{Cr}_2\text{AlC}$  could diffuse outwardly to the substrate alloy and  $\text{NiCrAlY}$  coating, which strengthened the metallurgical bonds at the interfaces between the substrate alloy and  $\text{Cr}_2\text{AlC}$  layer, as well as between the  $\text{Cr}_2\text{AlC}$  layer and  $\text{NiCrAlY}$  coating. However, due to the rapid outward diffusion of Al, the Al content in  $\text{Cr}_2\text{AlC}$

steadily decreased, leading to the phase transformation of  $\text{Cr}_2\text{AlC}$  to dense Cr–C compounds ( $\text{Cr}_7\text{C}_3$ ,  $\text{Cr}_{23}\text{C}_6$ ) on both sides of the transition layer. These Cr–C compounds are typical ceramic candidates for diffusion barriers. Moreover, Mourad *et al.*<sup>170</sup> demonstrated the thermodynamic, dynamic and mechanical stability of  $\text{Hf}_2\text{GeX}$  (X = C, N, and B) 211 MAX phases through a first-principles investigation, which displayed that they were likely to have thermal barrier coating applications.

## 5. Summary and outlook

To summarize, this report reviews the development, chemical compositions, and microstructures of MAX phase coatings, as well as various synthesis techniques such as PVD, CVD, spraying methods, and laser cladding. It also surveys the protective performances of MAX phase coatings and explores their potential functional applications. Thanks to the dedicated efforts of material researchers, significant progress has been made in understanding and characterizing the microstructures and properties of MAX phases, discovering new coatings and identifying potential applications. However, there are still some issues which need to be solved or more deeply investigated.

To date, over 340 types of MAX phase materials have been synthesized, with most research focusing on bulk materials and powder preparation. Developing a wider range of MAX phase coating systems, including MAX phase solid solutions, is crucial for expanding the research and functional applications of MAX phase materials. Although many MAX phases have been theoretically predicted to be thermodynamically and mechanically stable, their experimental realization remains challenging due to immature synthesis techniques. Achieving high-purity MAX phases is particularly difficult, complicating accurate property characterization. Consequently, improving the purity of MAX phase coatings using existing synthesis methods, as well as developing novel synthesis techniques, remains a key priority. Moreover, further research is needed to elucidate the microstructure–property relationships of MAX phases. For instance, the stability of MAX phases with atomic vacancies requires deeper investigation, as it can provide valuable insight into their application as high temperature oxidation resistance and self-healing materials. Additionally, a wide range of chemical and physical properties of the newly developed MAX phase coatings await further characterization. In particular, the magnetic properties of MAX phases and their solid solutions demand attention, including the effects of atomic configuration, alloy composition, temperature, magnetic fields, and applied pressure. Finally, developing commercially viable applications for MAX phase materials is an urgent priority, as successful market penetration could significantly stimulate further research and development. The potential applications for this family of layered metallic ceramics are vast, and their commercialization could revolutionize multiple industries.

## Author contributions

Guanshui Ma: conceptualization, investigation, writing – review & editing, project administration, and funding acquisition.

Anfeng Zhang: investigation and writing – original draft. Zhenyu Wang: resources, writing – review & editing, project administration, and funding acquisition. Kaihang Wang: investigation and writing – original draft. Jiayue Zhang: investigation and writing – original draft. Kaixuan Xu: investigation and writing – original draft. Yuxi Xu: investigation and writing – review & editing. Shenghao Zhou: investigation and writing – original draft. Aiyang Wang: resources, writing – review & editing, project administration, and funding acquisition.

## Data availability

All data sets and research materials used in this review are cited appropriately and can be accessed through the respective publishers or repositories. For any additional information or specific inquiries about the data used in this review, please contact the corresponding author. Data will be shared in compliance with the relevant institutional and ethical guidelines, ensuring they are used solely for academic and research purposes.

## Conflicts of interest

The authors declare no competing interests.

## Acknowledgements

This work was supported by the financial support from the National Science Fund for Distinguished Young Scholars of China (52025014), the National Natural Science Foundation of China (52171090, 52101109), the Zhejiang Provincial Natural Science Foundation of China (LD24E010003), and the Natural Science Foundation of Ningbo (2023QL049, 2023J410). We are also very grateful to Yingjie Wang, Yan Zhang, and Kaiwei Yang for their help in writing this manuscript.

## References

- V. H. Nowotny, *Solid State Chem.*, 1971, **5**, 27–70.
- M. W. Barsoum and T. El-Raghy, *J. Am. Ceram. Soc.*, 1996, **79**, 1953–1956.
- J. C. Schuster, H. Nowotny and C. Vaccaro, *J. Solid State Chem.*, 1980, **32**, 213–219.
- M. W. Barsoum, *Solid State Chem.*, 2000, **28**, 201–281.
- M. Naguib, M. Kurtoglu, V. Presser, J. Lu, J. Niu, M. Heon, L. Hultman, Y. Gogotsi and M. W. Barsoum, *Adv. Mater.*, 2011, **23**, 4248–4253.
- W. Eom, H. Shin, W. Jeong, R. B. Ambade, H. Lee and T. H. Han, *Mater. Horiz.*, 2023, **10**, 4892–4902.
- W. T. Cao, W. Feng, Y. Y. Jiang, C. Ma, Z. F. Zhou, M.-G. Ma, Y. Chen and F. Chen, *Mater. Horiz.*, 2019, **6**, 1057–1065.
- N. Liu, J. Yuan, X. Zhang, Y. Ren, F. Yu and J. Ma, *Mater. Horiz.*, 2024, **11**, 1223–1233.
- L. Ma, L. F. Wei, M. Hamidinejad and C. B. Park, *Mater. Horiz.*, 2023, **10**, 4423–4437.
- S. Zhang, X. Xu, X. Liu, Q. Yang, N. Shang, X. Zhao, X. Zang, C. Wang, Z. Wang, J. G. Shapter and Y. Yamauchi, *Mater. Horiz.*, 2022, **9**, 1708–1716.
- Q. Z. Tao, M. Dahlqvist, J. Lu, S. Kota, R. Meshkian, J. Halim, J. Palisaitis, L. Hultman, M. W. Barsoum, P. O. Å. Persson and J. Rosen, *Nat. Commun.*, 2017, **8**, 14949.
- L. Chen, M. Dahlqvist, T. Lapauw, B. Tunca, F. Wang, J. Lu, R. Meshkian, K. Lambrinou, B. Blanpain, J. Vleugels and J. Rosen, *Inorg. Chem.*, 2018, **57**, 6237–6244.
- X. Feng, N. Li, B. Chen, C. Zeng, T. Bai, K. Wu, Y. Cheng and B. Xiao, *J. Mater. Sci. Technol.*, 2023, **134**, 81–88.
- M. Ade and H. Hillebrecht, *Inorg. Chem.*, 2015, **54**, 6122–6135.
- J. Wang, T. N. Ye, Y. Gong, J. Wu, N. Miao, T. Tada and H. Hosono, *Nat. Commun.*, 2019, **10**, 2284.
- T. Rackl, L. Eisenburger, R. Niklaus and D. Johrendt, *Phys. Rev. Mater.*, 2019, **3**, 054001.
- M. Li, J. Lu, K. Luo, Y. Li, K. Chang, K. Chen, J. Zhou, J. Rosen, L. Hultman, P. Eklund, P. O. Å. Persson, S. Du, Z. Chai, Z. Huang and Q. Huang, *J. Am. Chem. Soc.*, 2019, **141**, 4730–4737.
- H. M. Ding, Y. Li, J. Lu, K. Luo, K. Chen, M. Li, P. O. Å. Persson, L. Hultman, P. Eklund, S. Du, Z. Huang, Z. Chai, H. Wang, P. Huang and Q. Huang, *Mater. Res. Lett.*, 2019, **7**, 510–516.
- M. Griseri, B. Tunca, S. G. Huang, M. Dahlqvist, J. Rosén, J. Lu, P. O. Å. Persson, L. Popescu, J. Vleugels and K. Lambrinou, *Science*, 2020, **40**, 1829–1838.
- P. P. Michalowski, M. Anayee, T. S. Mathis, S. Kozdra, A. Wojcik, K. Hantanasirisakul, I. Jozwik, A. Piatkowska, M. Mozdzonek, A. Malinowska, R. Didusko, E. Wierzbicka and Y. Gogotsi, *Nat. Nanotechnol.*, 2022, **17**, 1192–1197.
- Q. Wang, L. Velasco, B. Breitung and V. Presser, *Adv. Energy Mater.*, 2021, **11**, 2102355.
- J. Zhou, Q. Tao, B. Ahmed, J. Palisaitis, I. Persson, J. Halim, M. W. Barsoum, P. O. Å. Persson and J. Rosen, *Chem. Mater.*, 2022, **34**, 2098–2106.
- J. B. Shen, M. Zhang, S. Lin, W. Song, H. Liu, Q. Liu, X. Zhu and Y. Sun, *J. Appl. Phys.*, 2023, **133**, 235101.
- S. Schweidler, M. Botros, F. Strauss, Q. Wang, Y. Ma, L. Velasco, G. Cadilha Marques, A. Sarkar, C. Kübel, H. Hahn, J. Aghassi-Hagmann, T. Brezesinski and B. Breitung, *Nat. Rev. Mater.*, 2024, **9**, 266–281.
- Z. Wu, X. Zhu, Y. Shen, X. Zong, Y. Wu, Q. Wang, J. Tang, Z. Wang, H. Zhu, X. Yuan, Z. Zhou, X. Liu, X. Zhang, H. Wang, S. Jiang, M. J. Kim and Z. Lu, *Mater. Today*, 2024, **80**, 61–73.
- C. Liu, Y. Y. Yang, Z. F. Zhou, C. W. Nan and Y. H. Lin, *J. Am. Ceram. Soc.*, 2021, **105**, 2764–2771.
- L. Qiao, J. Bi, G. Liang, C. Liu, Z. Yin, Y. Yang, H. Wang, S. Wang, M. Shang and W. Wang, *J. Mater. Sci. Technol.*, 2023, **137**, 112–122.
- G. He, Y. Zhang, P. Yao, X. Li, K. Ma, J. Zuo, M. Li, C. Liu and J. Xu, *J. Mater. Sci. Technol.*, 2023, **137**, 91–99.
- W. Bao, X. G. Wang, H. Ding, P. Lu, C. Zhu, G. J. Zhang and F. Xu, *Scr. Mater.*, 2020, **183**, 33–38.



- 30 H. M. Ding, Y. B. Li, K. Chen, K. Liang, G. X. Chen, J. Lu, J. Palisaitis, P. O. Å. Persson, P. Eklund, L. Hultman, S. Du, Z. F. Chai, Y. Gogotsi and Q. Huang, *Science*, 2023, **379**, 1130–1135.
- 31 M. Dahlqvist, M. W. Barsoum and J. Rosen, *Mater. Today*, 2024, **72**, 1–24.
- 32 Z. Zhang, X. Duan, D. Jia, Y. Zhou and S. Zwaag, *J. Eur. Ceram. Soc.*, 2021, **41**, 3851–3878.
- 33 N. Goossens, B. Tunca, T. Lapauw, K. Lambrinou and J. Vleugels, *Encyclopedia of Materials: Technical Ceramics and Glasses*, 2021, vol. 2, pp. 182–199.
- 34 Z. M. Sun, *Int. Mater. Rev.*, 2013, **56**, 143–166.
- 35 L. Fu and W. Xia, *Adv. Eng. Mater.*, 2021, **23**, 2001191.
- 36 Z. Lin, M. Zhuo, Y. Zhou, M. Li and J. Wang, *J. Am. Ceram. Soc.*, 2006, **89**, 3765–3769.
- 37 J. P. Palmquist, S. Li, P. O. Å. Persson, J. Emmerlich, O. Wilhelmsson, H. Högberg, M. I. Katsnelson, B. Johansson, R. Ahuja, O. Eriksson, L. Hultman and U. Jansson, *Phys. Rev. B: Condens. Matter Mater. Phys.*, 2004, **70**, 165401.
- 38 M. Uddin, Md., M. A. Ali and M. S. Ali, Structural, elastic, electronic and optical properties of metastable MAX phase  $\text{Ti}_5\text{SiC}_4$  compound, *Indian J. Pure Appl. Phys.*, 2016, **54**, 386–390.
- 39 J. Lyu, E. B. Kashkarov, N. Travitzky, M. S. Syrtanov and A. M. Lider, *J. Mater. Sci.*, 2020, **56**, 1980–2015.
- 40 M. J. Peng, Y. C. Guo, A. C. Yang, Y. H. Duan, H. M. Yang, Y. J. Wu and M. N. Li, *Indian J. Phys.*, 2024, **98**, 3165–3177.
- 41 Y. Bai, N. Srikanth, C. K. Chua and K. Zhou, *Crit. Rev. Solid State Mater. Sci.*, 2017, **44**, 56–107.
- 42 E. Y. Andrei and A. H. MacDonald, *Nat. Mater.*, 2021, **20**, 571.
- 43 W. B. Yu, W. Z. Jia, F. Guo, Z. Y. Ma, P. C. Zhang, C. Tromas, V. Gauthier-Brunet, P. R. C. Kent, W. W. Sun and S. Dubois, *J. Eur. Ceram. Soc.*, 2020, **40**, 2279–2286.
- 44 A. Shamsipoor, M. Farvizi, M. Razavi, A. Keyvani, B. Mousavi and W. Pan, *Ceram. Int.*, 2021, **47**, 2347–2357.
- 45 C. X. Wang, T. F. Yang, C. L. Tracy, J. R. Xiao, S. S. Liu, Y. Fang, Z. F. Yan, W. Ge, J. M. Xue, J. Zhang, J. Y. Wang, Q. Huang, R. C. Ewing and Y. G. Wang, *Acta Mater.*, 2018, **144**, 432–446.
- 46 C. Wang, T. Yang, J. Xiao, S. Liu, J. Xue, Q. Huang, J. Zhang, J. Wang, Y. Wang and R. Koc, *J. Am. Ceram. Soc.*, 2016, **99**, 1769–1777.
- 47 D. W. Clark, S. J. Zinkle, M. K. Patel and C. M. Parish, *Acta Mater.*, 2016, **105**, 130–146.
- 48 C. Wang, T. Yang, J. Xiao, S. Liu, J. Xue, J. Wang, Q. Huang and Y. Wang, *Acta Mater.*, 2015, **98**, 197–205.
- 49 Z. Y. Wang, G. S. Ma, Z. Li, H. Ruan, J. H. Yuan, L. Wang, P. L. Ke and A. Y. Wang, *Corros. Sci.*, 2021, **192**, 109788.
- 50 C. Guo, X. Duan, Z. Fang, Y. Zhao, T. Yang, E. H. Wang and X. M. Hou, *Acta Mater.*, 2022, **241**, 118378.
- 51 W. B. Tian, P. L. Wang, G. J. Zhang, Y. M. Kan and Y. X. Li, *J. Am. Ceram. Soc.*, 2007, **90**, 1663–1666.
- 52 M. Rougab and A. Gueddouh, *Comput. Theor. Chem.*, 2024, **1233**, 114497.
- 53 L. O. Xiao, S. B. Li, G. Song and W. G. Sloof, *J. Eur. Ceram. Soc.*, 2011, **31**, 1497–1502.
- 54 D. J. Tallman, E. N. Hoffman, E. A. N. Caspi, B. L. Garcia-Diaz, G. Kohse, R. L. Sindelar and M. W. Barsoum, *Acta Mater.*, 2015, **85**, 132–143.
- 55 A. Biswas, V. Natsu and A. B. Puthirath, *Oxford Open Mater. Sci.*, 2021, **1**, 1–11.
- 56 C. Wang, T. Yang, S. Kong, J. Xiao, J. Xue, Q. Wang, C. Hu, Q. Huang and Y. Wang, *J. Nucl. Mater.*, 2013, **440**, 606–611.
- 57 J. L. Lu, N. Abbas, J. Tang, R. Hu and G. M. Zhu, *Electrochem. Commun.*, 2019, **105**, 106490.
- 58 J. L. Lu, N. Abbas, J. N. Tang, J. Tang and G. M. Zhu, *Corros. Sci.*, 2019, **158**, 108106.
- 59 J. H. Yuan, Z. Y. Wang, G. S. Ma, X. J. Bai, Y. Li, X. Cheng, P. L. Ke and A. Y. Wang, *J. Mater. Sci. Technol.*, 2023, **143**, 140–152.
- 60 Q. M. Wang, R. Mykhalonka, A. Flores Renteria, J. L. Zhang, C. Leyens and K. H. Kim, *Corros. Sci.*, 2010, **52**, 3793–3802.
- 61 Q. M. Wang, A. Flores Renteria, O. Schroeter, R. Mykhalonka, C. Leyens, W. Garkas and M. to Baben, *Surf. Coat. Technol.*, 2010, **204**, 2343–2352.
- 62 R. Grieseler, B. Hähnlein, M. Stubenrauch, T. Kups, M. Wilke, M. Hopfeld, J. Pezoldt and P. Schaaf, *Appl. Surf. Sci.*, 2014, **292**, 997–1001.
- 63 Y. Li, G. Zhao, Y. Qian, J. Xu and M. Li, *Vacuum*, 2018, **153**, 62–69.
- 64 N. Abbas, X. Qin, S. Ali, G. Zhu, J. Lu, F. E. Alam, A. G. Wattoo, X. Zeng, K. Gu and J. Tang, *J. Eur. Ceram. Soc.*, 2020, **40**, 3338–3342.
- 65 V. Stranak, J. Kratochvil, J. Olejnicek, P. Ksirova, P. Sezemsky, M. Cada and Z. Hubicka, *J. Appl. Phys.*, 2017, **121**, 171914.
- 66 X. Zuo, D. Zhang, R. D. Chen, P. L. Ke, M. Odén and A. Y. Wang, *Plasma Sources Sci. Technol.*, 2020, **29**, 015013.
- 67 Z. C. Li, G. X. Zhou, Z. Y. Wang, J. H. Yuan, P. L. Ke and A. Y. Wang, *J. Eur. Ceram. Soc.*, 2023, **43**, 4673–4683.
- 68 T. F. Zhang, Q. M. Wang, J. Lee, P. Ke, R. Nowak and K. H. Kim, *Surf. Coat. Technol.*, 2012, **212**, 199–206.
- 69 G. X. Zhou, Z. Li, J. H. Yuan, R. D. Chen, Z. Y. Wang, P. L. Ke and A. Y. Wang, *Appl. Surf. Sci.*, 2024, **666**, 160371.
- 70 D. W. Zhou, Z. Z. Li, Z. Y. Wang, G. S. Ma, P. L. Ke, X. J. Hu and A. Y. Wang, *China Surf. Eng.*, 2022, **35**, 236–245.
- 71 M. W. Qureshi, X. Ma, G. Tang, B. Miao and J. Niu, *Materials*, 2021, **14**, 826.
- 72 D. M. Sanders and A. Anders, *Surf. Coat. Technol.*, 2000, **133**, 78–90.
- 73 J. Rosén, L. Ryves, P. O. Å. Persson and M. M. M. Bilek, *J. Appl. Phys.*, 2007, **101**, 056101.
- 74 H. Li, H. S. Cao, F. J. Liu, Y. H. Li, F. G. Qi, X. P. Ouyang and N. Zhao, *J. Eur. Ceram. Soc.*, 2022, **42**, 2073–2083.
- 75 M. C. Guenette, M. D. Tucker, M. Ionescu, M. M. M. Bilek and D. R. McKenzie, *Thin Solid Films*, 2010, **519**, 766–769.
- 76 Z. Mahmoudi, S. H. Tabaian, H. R. Rezaie, F. Mahboubi and M. J. Ghazali, *Ceram. Int.*, 2020, **46**, 4968–4975.
- 77 G. S. Ma, J. H. Yuan, R. D. Chen, H. Li, H. C. Wu, J. S. Yan, Z. Y. Wang and A. Y. Wang, *Appl. Surf. Sci.*, 2022, **597**, 153670.

- 78 G. S. Ma, D. Zhang, P. Guo, H. Li, Y. Xin, Z. Y. Wang and A. Y. Wang, *J. Mater. Sci. Technol.*, 2022, **105**, 36–44.
- 79 Z. Y. Wang, G. S. Ma, L. Liu, L. Wang, P. L. Ke, Q. Xue and A. Y. Wang, *Corros. Sci.*, 2020, **167**, 108492.
- 80 Z. Y. Wang, W. Li, Y. Liu, J. T. Shuai, P. L. Ke and A. Y. Wang, *Appl. Surf. Sci.*, 2020, **502**, 144130.
- 81 A. R. Phani, J. E. Krzanowski and J. J. Nainaparampil, *J. Vac. Sci. Technol., A*, 2001, **19**, 2252–2258.
- 82 J. J. Hua, J. E. Bultman, S. Patton and J. S. Zabinski, *Tribol. Lett.*, 2004, **16**, 113–122.
- 83 C. Lange, M. Hopfeld, M. Wilke, J. Schawohl, T. Kups, M. W. Barsoum and P. Schaaf, *Phys. Status Solidi A*, 2011, **209**, 545–552.
- 84 Z. J. Feng, P. L. Ke and A. Y. Wang, *J. Mater. Sci. Technol.*, 2015, **31**, 1193–1197.
- 85 G. S. Ma, H. C. Wu, Z. Fang, X. H. Zhou, R. D. Chen, W. Yang, J. Zhang, Z. Y. Wang and A. Y. Wang, *J. Mater. Sci. Technol.*, 2025, **206**, 176–184.
- 86 M. Bahiraei, Y. Mazaheri, M. Sheikhi and A. Heidarpour, *Surf. Coat. Technol.*, 2020, **385**, 125314.
- 87 J. J. Nickl, K. K. Schweitzer and P. Luxenberg, *J. Less-Common Met.*, 1972, **26**(3), 335–353.
- 88 C. Racautl, F. Langlais and R. Naslain, *J. Mater. Sci. Technol.*, 1994, **29**, 3941–3948.
- 89 E. Pickering, W. J. Lackey and S. Crain, *Chem. Vap. Deposition*, 2000, **6**, 289–295.
- 90 V. K. Champagne, *Handbook the Cold Spray Materials Deposition Process*, Woodhead Publishing and Maney Publishing on behalf of The Institute of Materials, Minerals & Mining, 2007.
- 91 X. Lei and N. M. Lin, *Crit. Rev. Solid State Mater. Sci.*, 2022, **47**, 736–771.
- 92 J. Frodelius, M. Sonestedt, S. Björklund, J. P. Palmquist, K. Stiller, H. Högberg and L. Hultman, *Surf. Coat. Technol.*, 2008, **202**, 5976–5981.
- 93 H. Gutzmann, F. Gärtner, D. Höche, C. Blawert and T. Klassen, *J. Therm. Spray Technol.*, 2012, **22**, 406–412.
- 94 B. R. Maier, B. L. Garcia-Diaz, B. Hauch, L. C. Olson, R. L. Sindelar and K. Sridharan, *J. Nucl. Mater.*, 2015, **466**, 712–717.
- 95 H. K. H. Assadi, F. Gärtner and T. Klassen, *Acta Mater.*, 2016, **116**, 382–407.
- 96 W. Zhang, S. Li, X. Zhang and X. Chen, *Coatings*, 2023, **13**, 869.
- 97 P. Richardson, D. Cuskelly, M. Brandt and E. Kisi, *Surf. Coat. Technol.*, 2020, **385**, 125360.
- 98 Y. X. Tian, H. Q. Xiao, L. R. Ren, J. Y. Feng, Y. Xiao, N. Chen and X. Zhou, *Surf. Coat. Technol.*, 2022, **448**, 128944.
- 99 T. Galvin, N. C. Hyatt, W. M. Rainforth, I. M. Reaney and D. Shepherd, *Surf. Coat. Technol.*, 2019, **366**, 199–203.
- 100 E. I. Zamulaeva, E. A. Levashov, T. A. Sviridova, N. V. Shvyndina and M. I. Petrzhik, *Surf. Coat. Technol.*, 2013, **235**, 454–460.
- 101 M. Haftani, M. Saeedi Heydari, H. R. Baharvandi and N. Ehsani, *Int. J. Refract. Met. Hard Mater.*, 2016, **61**, 51–60.
- 102 Z. Zhang, D. M. Y. Lai, S. H. Lim, H. Jin, S. Wang, J. Chai and J. Pan, *J. Alloys Compd.*, 2019, **790**, 536–546.
- 103 N. Laska, R. Swadźba, P. Nellessen, O. Helle and R. Anton, *Surf. Coat. Technol.*, 2024, **480**, 130601.
- 104 Y. Xiao, H. Xiao, T. Mo, L. Ren, Y. Tian and L. Zhu, *Ceram. Int.*, 2023, **49**, 38672–38682.
- 105 Y. Li, J. J. Xu, J. J. Li, Y. M. Li, K. Ma, W. T. Wang, X. T. Zhang, Y. Zhang and M. S. Li, *Corros. Sci.*, 2023, **222**, 111416.
- 106 L. Mengis, C. Oskay, N. Laska and M. C. Galetz, *Intermetallics*, 2023, **163**, 108039.
- 107 J. J. Li, M. S. Li, H. M. Xiang, X. P. Lu and Y. C. Zhou, *Corros. Sci.*, 2011, **53**, 3813–3820.
- 108 J. Li, H. Xiang, J. Xu, L. Zheng and Y. Qian, *Surf. Coat. Technol.*, 2021, **422**, 127554.
- 109 X. Chen, B. Stelzer, M. Hans, R. Iskandar, J. Mayer and J. M. Schneider, *Mater. Res. Lett.*, 2020, **9**, 127–133.
- 110 C. Tang, M. Große, S. Ulrich, M. Klimenkov, U. Jäntschi, H. J. Seifert, M. Stüber and M. Steinbrück, *Surf. Coat. Technol.*, 2021, **419**, 127263.
- 111 Z. C. Li, Z. Y. Wang, G. S. Ma, R. D. Chen, W. Yang, K. H. Wang, P. L. Ke and A. Y. Wang, *Corros. Commun.*, 2024, **13**, 27–36.
- 112 Z. J. Feng, P. L. Ke, Q. Huang and A. Y. Wang, *Surf. Coat. Technol.*, 2015, **272**, 380–386.
- 113 W. T. Li, Z. Y. Wang, J. T. Shuai, B. B. Xu, A. Y. Wang and P. L. Ke, *Ceram. Int.*, 2019, **45**, 13912–13922.
- 114 A. Hesnawi, H. Li, Z. Zhou, S. Gong and H. Xu, *Vacuum*, 2007, **81**, 947–952.
- 115 Z. Y. Wang, J. Sun, B. B. Xu, Y. R. Liu, P. L. Ke and A. Y. Wang, *J. Eur. Ceram. Soc.*, 2020, **40**, 197–201.
- 116 A. S. Farle, C. Kwakernaak, S. Zwaag and W. G. Sloof, *J. Eur. Ceram. Soc.*, 2015, **35**, 37–45.
- 117 J. Wang, X. Wang, Y. Zhang, G. Bai, J. Zhang and Y. Lei, *J. Inorg. Mater.*, 2021, **36**, 1097–1102.
- 118 D. J. Tallman, B. Anasori and M. W. Barsoum, *Mater. Res. Lett.*, 2013, **1**, 115–125.
- 119 L. Guo, Y. Li and G. Li, *J. Adv. Ceram.*, 2023, **12**, 1712–1730.
- 120 J. Fu, T. F. Zhang, Q. Xia, S. H. Lim, Z. Wan, T. W. Lee and K. H. Kim, *J. Nanomater.*, 2015, **2015**, 1–12.
- 121 X. Li, S. Wang, G. Wu, D. Zhou, J. Pu, M. Yu, Q. Wang and Q. Sun, *Ceram. Int.*, 2022, **48**, 26618–26628.
- 122 Z. C. Li, Y. Zhang, K. H. Wang, Z. Y. Wang, G. S. Ma, P. L. Ke and A. Y. Wang, *Corros. Sci.*, 2024, **228**, 111820.
- 123 M. Zhu, R. Wang, C. Chen, H. B. Zhang and G. J. Zhang, *Ceram. Int.*, 2017, **43**, 5708–5714.
- 124 Y. Zhang, A. F. Zhang, Z. C. Li, Z. Y. Wang, P. L. Ke and A. Y. Wang, *J. Phys. Chem. C*, 2024, **128**, 3916–3923.
- 125 Z. Zhang, Y. Qian, J. Xu, J. Zuo and M. Li, *Corros. Sci.*, 2021, **178**, 109062.
- 126 H. Shi, R. Azmi, L. Han, C. Tang, A. Weisenburger, A. Heinzl, J. Maibach, M. Stüber, K. Wang and G. Müller, *Corros. Sci.*, 2022, **201**, 110275.
- 127 F. Zakeri-Shahroudi, B. Ghasemi, H. Abdolahpour and M. Razavi, *J. Mater. Eng. Perform.*, 2023, **23**, 1–13.
- 128 M. W. Barsoum and M. Radovic, *Annu. Rev. Mater. Res.*, 2011, **41**, 195–227.
- 129 M. Naveed, A. Obrosof, A. Zak, W. Dudzinski, A. Volinsky and S. Weiß, *Metals*, 2016, **6**, 265.

- 130 Y. L. Du, Z. M. Sun, H. Hashimoto and M. W. Barsoum, *J. Appl. Phys.*, 2011, **109**, 063707.
- 131 D. Eichner, A. Schlieter, C. Leyens, L. Shang, S. Shayestehaminzadeh and J. M. Schneider, *Wear*, 2018, **403**, 187–195.
- 132 X. Wei, L. Li, Y. Wu and F. Liu, *Mater. Today Commun.*, 2023, **35**, 105907.
- 133 J. J. Liu, X. Zuo, Z. Y. Wang, L. Wang, X. C. Wu, P. L. Ke and A. Y. Wang, *J. Alloys Compd.*, 2018, **753**, 11–17.
- 134 H. Rueß, J. Werner, Y. Unutulmazsoy, J. W. Gerlach, X. Chen, B. Stelzer, D. Music, S. Kolozsvári, P. Polcik, T. E. Weirich and J. M. Schneider, *J. Eur. Ceram. Soc.*, 2021, **41**, 1841–1847.
- 135 B. Völker, B. Stelzer, S. Mráz, H. Rueß, R. Sahu, C. Kirchlechner, G. Dehm and J. M. Schneider, *Mater. Design*, 2021, **206**, 109757.
- 136 J. Molina-Aldareguia, *Scr. Mater.*, 2003, **49**, 155–160.
- 137 J. H. Yuan, S. H. Zhou, H. C. Wu, Z. Y. Wang, Y. Zhang, G. X. Zhou, G. S. Ma, P. L. Ke and A. Y. Wang, *Scr. Mater.*, 2023, **235**, 115594.
- 138 C. Tang, M. Klimenkov, U. Jaentsch, H. Leiste, M. Rinke, S. Ulrich, M. Steinbrück, H. J. Seifert and M. Stueber, *Surf. Coat. Technol.*, 2017, **309**, 445–455.
- 139 F. Y. Zhang, G. X. Yu, S. Yan, J. W. Chen, H. L. Ma, J. N. He and F. X. Yin, *Ceram. Int.*, 2022, **48**, 26063–26071.
- 140 F. Y. Zhang, J. Chen, S. Yan, G. X. Yu, H. L. Ma, J. J. He and F. X. Yin, *Surf. Coat. Technol.*, 2022, **441**, 128584.
- 141 H. Li, H. Cao, J. Yang, Y. Li, F. Qi, N. Zhao and X. Ouyang, *Mater. Charact.*, 2022, **194**, 112421.
- 142 F. Zhang, C. Li, S. Yan, J. He and F. Yin, *Ceram. Int.*, 2021, **47**, 3173–3184.
- 143 C. Wang, H. Tu, R. Su, J. Gao, B. V. King, D. J. O'Connor and L. Shi, *J. Am. Ceram. Soc.*, 2020, **104**, 593–603.
- 144 C. Azina and P. Eklund, *Results Mater.*, 2021, **9**, 100159.
- 145 C. Azina, B. Tunca, A. Petruhins, B. Xin, M. Yildizhan, P. O. Å. Persson, J. Vleugels, K. Lambrinou, J. Rosen and P. Eklund, *Appl. Surf. Sci.*, 2021, **551**, 149370.
- 146 C. Azina, T. Bartsch, D. M. Holzapfel, M. Dahlqvist, J. Rosen, L. Löffler, A. S. J. Mendez, M. Hans, D. Primetzhofer and J. M. Schneider, *J. Am. Ceram. Soc.*, 2022, **106**, 2652–2665.
- 147 Z. Y. Wang, C. C. Wang, Y. Zhang, A. Y. Wang and P. L. Ke, *Mater. Design*, 2022, **222**, 111060.
- 148 Y. Wang, D. F. Ruiz Diaz, K. S. Chen, Z. Wang and X. C. Adroher, *Mater. Today*, 2020, **32**, 178–203.
- 149 Y. S. Song and Y. J. Park, *Endocrinol Metab*, 2019, **34**, 1–10.
- 150 R. Y. Liu, J. Chen, L. B. Zhou, W. Qiu, W. Y. Huang and Y. Niu, *J. Chinese. Soc. Corros. Prot.*, 2023, **43**, 62–68.
- 151 C. Wang, C. L. Tracy and R. C. Ewing, *Appl. Phys. Rev.*, 2020, **7**, 041311.
- 152 C. Wang, Z. Han, R. Su, J. Gao and L. Shi, *Nucl. Instrum. Methods Phys. Res., Sect. B*, 2019, **450**, 286–290.
- 153 R. Su, H. Zhang, L. Liu, L. Shi and H. Wen, *J. Eur. Ceram. Soc.*, 2021, **41**, 6309–6318.
- 154 M. Imtyazuddin, A. H. Mir, M. A. Tunes and V. M. Vishnyakov, *J. Nucl. Mater.*, 2019, **526**, 151742.
- 155 M. Imtyazuddin, A. H. Mir, E. Aradi and V. Vishnyakov, *Nanotechnology*, 2020, **31**, 385602.
- 156 C. Tang, M. K. Grosse, P. Trtik, M. Steinbrück, M. Stüber and H. J. Seifert, *Acta Polytech.*, 2018, **58**, 69–76.
- 157 E. N. Hoffman, D. W. Vinson, R. L. Sindelar, D. J. Tallman, G. Kohse and M. W. Barsoum, *Nucl. Eng. Des.*, 2012, **244**, 17–24.
- 158 M. Bugnet, V. Mauchamp, E. Oliviero, M. Jaouen and T. Cabioc'h, *J. Nucl. Mater.*, 2013, **441**, 133–137.
- 159 M. A. Tunes, M. Imtyazuddin, C. Kainz, S. Pogatscher and V. M. Vishnyakov, *Sci. Adv.*, 2021, **7**, 1–12.
- 160 D. Bowden, J. Ward, S. Middleburgh, S. Moraes Shubeita, E. Zapata-Solvas, T. Lapauw, J. Vleugels, K. Lambrinou, W. E. Lee, M. Preuss and P. Frankel, *Acta Mater.*, 2020, **183**, 24–35.
- 161 W. Ling, K. Lai, J. Chen, F. Guo, D. Kang, Z. Zhao and J. Dai, *Nucl. Mater. Energy*, 2023, **36**, 101486.
- 162 W. D. Ling, P. Wei, D. Q. Zhao, Y. P. Shao, J. Z. Duan, J. F. Han and W. S. Duan, *Phys. B*, 2019, **552**, 178–183.
- 163 Y. Liu, X. Jian, X. Su, F. Luo, J. Xu, J. Wang, X. He and Y. Qu, *J. Alloys Compd.*, 2018, **740**, 68–76.
- 164 Y. Liu, J. Yang, J. Xu, L. Lu and X. Su, *J. Alloys Compd.*, 2022, **899**, 163327.
- 165 J. Su, W. Zhou, Y. Liu, Y. Qing, F. Luo and D. Zhu, *Surf. Coat. Technol.*, 2015, **270**, 39–46.
- 166 J. W. Huang, J. Hu, M. Z. Li, M. Yi, J. L. Zhu, W. Shui, Y. F. Li, Q. Wen and X. H. Xiao, *J. Adv. Ceram.*, 2021, **10**, 1291–1298.
- 167 T. Go, Y. J. Sohn, G. Mauer, R. Vaßen and J. Gonzalez-Julian, *J. Eur. Ceram. Soc.*, 2019, **39**, 860–867.
- 168 J. Gonzalez-Julian, G. Mauer, D. Sebold, D. E. Mack and R. Vassen, *J. Am. Ceram. Soc.*, 2019, **103**, 2362–2375.
- 169 Y. Li, K. Ma, J. J. Xu, J. J. Li, Y. M. Li, Y. Zhang, J. Zuo and M. S. Li, *Corros. Sci.*, 2024, **226**, 111696.
- 170 M. Rougab and A. Gueddouch, *J. Phys. Chem. Solids*, 2023, **176**, 111251.